A comparative study between Amontons-Coulomb and Dieterich-Ruina friction laws for the cyclic response of a single degree of freedom system

Cabboi, Alessandro; Marino, Luca; Cicirello, Alice

DOI
10.1016/j.euromechsol.2022.104737

Publication date
2022

Document Version
Final published version

Published in
European Journal of Mechanics A - Solids

European Journal of Mechanics / A Solids 96 (2022) 104737

Contents lists available at ScienceDirect

European Journal of Mechanics / A Solids

journal homepage: www.elsevier.com/locate/ejmsol

A comparative study between Amontons–Coulomb and Dieterich–Ruina friction laws for the cyclic response of a single degree of freedom system

Alessandro Cabboi *, Luca Marino, Alice Cicirello

Faculty of Civil Engineering and Geosciences, Department of Engineering Structures, Section of Mechanics and Physics of Structures, Delft University of Technology, Stevinweg 1, 2628CN Delft, NL, Netherlands

ARTICLE INFO

Keywords:
Stick–slip
Nonlinear vibration
Constitutive friction laws
Rate-and-state laws

ABSTRACT

This study aims at assessing the predictive performance of the Amontons–Coulomb law to reliably predict the cyclic response, inclusive of stick–slip, of a single degree of freedom system in contact with the ground through two versions (steady-state and rate-and-state) of a regularized Dieterich–Ruina law. The assessment is carried out by defining a cost function and a physics-based constraint that enable the identification of the corresponding optimal coefficients of the Amontons–Coulomb law through a multi-start constrained non-linear optimization. The comparative study starts with a sensitivity analysis, aimed at first identifying the most meaningful model parameters for the Dieterich–Ruina law. Subsequently, the cyclic dynamic responses provided by both friction laws are analysed for varying model parameters, and characteristic features are observed within the dynamic forcing–displacement graph and the friction force–velocity plot, that could be directly linked to one friction model or the other. The sensitivity analysis led to the definition of a cost function expressed in terms of the displacement and velocity response differences and a constraint based on the phase difference. The optimization study identified areas of the Dieterich–Ruina's parameter space for which the Amontons–Coulomb law can reliably be used to predict a cyclic stick–slip response. The relevance of these results with respect to problems of modelling and identification of friction are discussed.

1. Introduction

Structural joints and interfaces characterized by moving surfaces are present in many mechanical and natural systems, encompassing a large spectrum of applications including aerospace, civil engineering, geomechanics and biology. Regardless the field of application, the common goal concerning sliding systems is the development of efficient predictive tools for their fundamental understanding, design and maintenance. What makes this goal challenging is the multidisciplinary nature that characterizes problems in which sliding systems are involved, since their mechanical behaviour depends on the coupling between the surface properties (that changes over different length- and time-scales) and the bulk mechanics of the systems in contact. The multi-scale nature and the complex interconnectivity between these interface mechanisms make the modelling and especially the experimental characterization of interface mechanics and properties two of the most challenging tasks in engineering research, as highlighted in three review studies (Vanossi et al., 2013; Vakis et al., 2018; Meng et al., 2020). In all these studies, the modelling strategy tends towards the development of complex and high-fidelity models, encompassing aspects such as the accurate rough surface representation, the physics of lubrication and wear. However, it may often be more convenient to adopt phenomenological interface models, able to mimic the most significant sliding features occurring at an interface level. The latter models exhibit a good trade-off between simplicity and complexity, and are particularly powerful for engineering design purposes. Nonetheless, models of such kind need to be constantly validated.

Phenomenological or empirical interface laws are often derived through tailored and specific experiments, and are meant to encapsulate friction-related interface behaviour in an empirical and simplified fashion, in order to avoid the development of highly complex numerical models of the surfaces in contact. For the latter ones, the reader may refer to classical textbooks on computational contact mechanics (Laursen, 1998; Wriggers, 1998). The computational cost for highly complex numerical models becomes especially high for transient and periodic dynamic simulations relevant for energy dissipation, fretting fatigue and friction-induced vibration analysis. The Amontons–Coulomb law can be considered the first empirical friction law. It was originally deduced by observing the initiation of sliding of objects in stationary contact (Pitenis et al., 2014), and still is the one used in most studies concerning the analytical and computational aspect of dynamic

* Corresponding author.
E-mail addresses: A.Cabboi@tudelft.nl (A. Cabboi), l.marino-1@tudelft.nl (L. Marino), a.cicirello@tudelft.nl (A. Cicirello).

https://doi.org/10.1016/j.euromechsol.2022.104737
Received 26 March 2022; Received in revised form 3 June 2022; Accepted 8 July 2022
Available online 13 July 2022

systems affected by friction. For example, it has been employed for evaluating analytical solutions for sliding regimes and thresholds for the stick conditions of the steady-state behaviour of idealized dynamic systems (Den Hartog, 1931; Shaw, 1986; Hong and Liu, 2001; Marino and Cicirello, 2021), for developing numerical strategies for multiple stick conditions (Hong and Liu, 2000), for investigating stability analysis (Sorge, 2007) and chaotic predictions (Csernak and Licsko, 2021).

The widely used Amontons–Coulomb law is not able to capture a series of phenomena observed in laboratory experiments such as, among others, ageing of the contact area (Blau, 2009; Dieterich, 1979; Bureau et al., 2002), velocity dependence (Blau, 2009; Marone, 1998; Bar-Sinai et al., 2015; Cabboi et al., 2016; Cabboi and Woodhouse, 2018), time lag effect during a sliding regime (Cabboi et al., 2016; Cabboi and Woodhouse, 2018; Hess and Soom, 1990; Heslot et al., 1994; Van De Velde and De Baets, 1998; Wiercigroch et al., 1999), breakaway friction force dependence on the applied tangential force rate (Lampaert et al., 2004; Sun et al., 2015), and frequency dependence of the friction force due to dynamic perturbations (Cabboi et al., 2016; Cabboi and Woodhouse, 2018). To account of such effects at a macroscale level, phenomenological friction laws were developed over time, which are of paramount importance for the design and control of mechanical systems. Among these laws, the rate-and-state models (developed in the 70's within the geomechanic community (Dieterich, 1979; Ruina, 1983; Rice and Ben-Zion, 1996) and the LuGre model (Canudas de Wit et al., 1995) (proposed in the 90's by the control community) proved to be the most successful ones within their domain of application. Both models were gradually enhanced in time to cope with new experimental observations aiming to extend their domain of applicability. Examples for such enhanced models can be found in Bar-Sinai et al. (2015), Cabboi et al. (2016), Putelat and Dawes (2015), Gonthier et al. (2004), Jankowski et al. (2016), Al-Bender et al. (2005) and Marques et al. (2021).

The progressive enhancement of friction laws is a direct consequence of the absence of a general phenomenological law of friction. As a result, the level of complexity of the friction law employed is currently dependent on the type of problem and application. This implies that there is a continuous need to validate the friction laws for each type of applications, keeping in mind that friction models developed and validated for one application may not perform well for other ones (Woodhouse et al., 2015). However, for the above mentioned friction laws, neither regulated protocols or codes nor homologated tribometers do exist for validation purposes. To check out some examples of prototype tribometers capable of testing the multiple friction features mentioned above (except of the frequency dependence of the friction force) the reader may refer to Lampaert et al. (2004) and Sun et al. (2015). Given the large spectrum of friction models available, practitioners should be equipped with guidelines on which friction model to use for a given application, nevertheless, current engineering handbooks are still limited by referring to Amontons–Coulomb coefficients for different material combinations. On this regard, despite few studies (Sun et al., 2015; Woodhouse et al., 2015; Berger, 2002; Pennestrì et al., 2016; Marques et al., 2016) aiming at comparing different friction models in a systematic manner, the literature shows very little recognition about this key issue, especially if compared to the multitude of modelling problems encountered in engineering when friction needs to be taken into account.

It is worth mentioning Ref. (Pennestrì et al., 2016), in which eight well-known friction models used in engineering were reviewed and compared. The friction models were classified based on the Amontons–Coulomb viewpoint and the bristle analogy, accounting for the interface compliance. Three different test-cases were investigated: the spring–mass system on a moving belt (Rabinowicz test case), a three degrees of freedom system with multiple contacts and a pre-sliding test case constituted by a moving mass (for the latter see Dupont et al. (2002) as well for more details). The results of such study seem to favour the LuGre friction model (Canudas de Wit et al., 1995) (in combination with the Gonthier friction model (Gonthier et al., 2004), an extension of the LuGre model), that exhibited a good trade-off between simulating meaningful friction features and the computational cost. A conclusion along the same line was also drawn in Sun et al. (2015). For further and more challenging applications, such as transients predictions and stability analysis of friction-induced vibration phenomena, converging towards a reliable friction model is still an elusive task (Woodhouse et al., 2015). For example, in Cabboi and Woodhouse (2018) it was shown that the fluctuating friction force component between specific surfaces in contact exhibits a systematic frequency dependence that can be captured by a compliant rate-and-state friction model. Further attempts to reproduce the fluctuating friction force component consisted in adding an evolving perturbation term of the friction coefficient (Lacerra et al., 2018). This short overview highlights that to fairly assess the friction models and to understand under which operational conditions certain friction laws are more indicated then others, quantities and response features that are representative enough of the main friction-related effects characterizing the case at hand are needed. On such regard, the comparison of friction models has been carried out by investigating limit cycles (Liu and Wu, 2014), since the stability boundaries are highly sensitive to a change of the friction law. Nyquist plots of the frictional impedance function (Cabboi et al., 2016) were also used to discriminate among friction laws suitable for a complex eigenvalue analysis. Free dynamic decays (Rigaud et al., 2010; Le Bot et al., 2019) were used to evaluate the dependence or independence of friction from velocity, and quantities accounting for the energy dissipation per cycle (Lopez and Nijmeijer, 2009). When considering quasi-static loading, quantities such as the breakaway force, the friction lag and the pre-sliding behaviour (Sun et al., 2015) are usually investigated.

Within this context, it is the aim of the current paper to shed light on when the Amontons–Coulomb coefficients can be used as an equivalent friction law to reliably predict a stick–slip response, with reference to a specific model setup and an underlining assumed interface law, such as the Dieterich–Ruina friction law. The dynamic response of sliding systems is of paramount importance to assess the energy transmission and dissipation, relevant for applications such as friction dampers (Marino and Cicirello, 2021; Gastaldi and Gola, 2016; Gagnon et al., 2020). In a previous study, focused on quantifying the energy dissipation (Lopez and Nijmeijer, 2009) of a single degree of freedom (1-DOF) system (representing an idealized version of a friction damper) it was briefly concluded that friction models that differ from the Amontons–Coulomb law would not have a significant effect on the estimated dissipated energy. The following work is meant to systematically assess up to which extent the Amontons–Coulomb coefficients could be used, provided that the actual friction force is characterized by a more complex friction law. The present comparative study is focused on the cyclic response of a 1-DOF system influenced by frictional contact with the ground, including two stops and more than two stops during one cycle of motion as well. The reason of limiting the analysis to a 1-DOF system is merely due to the fact that eventual mismatches between the responses obtained by the assumed friction laws will only increase in case more degrees of freedoms are assumed (e.g. normal and tangential direction of motion). Specifically, the forced mass–spring system is assumed to be governed either by an Amontons–Coulomb law or by the Dieterich–Ruina law (Dieterich, 1979; Rice and Ben-Zion, 1996). The analysis of the dynamic responses allowed the identification of characteristic features observable within a representative response cycle and referable to the adopted friction laws. Concerning the Dieterich–Ruina law, its steady-state and rate-and-state version were assumed. The Dieterich–Ruina law is assumed as the predefined underlining constitutive law of friction, and an optimization study was then performed throughout a chosen parameter space of the Dieterich–Ruina model, to identify the optimal pair of Amontons–Coulomb friction coefficients able to accurately predict the cyclic response, inclusive of stick–slip. The Dieterich–Ruina law is

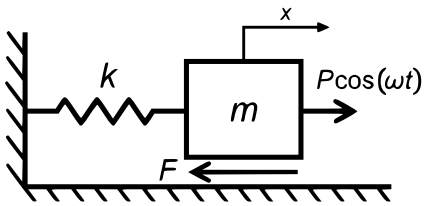

Fig. 1. Harmonically excited mass–spring system.

commonly used within the geomechanics community and has been only recently introduced for mechanical engineering applications such as the prediction of squeal phenomenon (Cabboi and Woodhouse, 2020). Besides the comparative analysis, this study also proposed a regularized version of the Dieterich–Ruina friction law, by eliminating the singularity at zero velocity and enabling its use for cases of velocity reversals. Throughout this study, it is shown that, for specific sets of model parameters of the Dieterich–Ruina law, the corresponding cyclic stick–slip response of 1-DOF oscillator characterized by a two-stop motion can be well represented by simply using a set of Amontons–Coulomb coefficients, namely the static one μ_s in combination with the kinetic one μ_k. The obtained results are of interest both for the interface characterization of sliding systems through tribological experiments, and also for the preliminary design phase of a sliding system subject to a vibratory force, for which idealized 1-DOF models may be justified (i.e., systems with well-separated modes and force spectrum localized around a single mode of vibration). As a final note, throughout the paper, we refer to expressions such as steady-state and cyclic dynamic responses. Steady-state refers to the dynamic friction law of the Dieterich–Ruina type for which the state variable is neglected, while cyclic response refers to a periodic cycle of a stick–slip motion.

2. Friction models and sensitivity analyses

To elucidate the effects on the dynamic response triggered by three different friction laws, a harmonically excited sliding mass–spring system is used. In Fig. 1, the single degree of freedom is represented by the displacement along the x direction, the spring stiffness is defined by k, the mass by m, while P and ω stand for the amplitude and frequency of the applied harmonic load. Two different constitutive laws for the friction force F are investigated: the Amontons–Coulomb law (Section 2.1), and a particular realization of a rate-and-state friction model (Section 2.2) provided by the Dieterich–Ruina law. For the latter friction law, a steady-state version was also used exhibiting only a friction force–velocity dependence. All friction laws are qualitatively illustrated in Fig. 2. The Amontons–Coulomb law can either be defined by assuming a single value friction coefficient or a distinction can be made between a static, μ_s, and a kinetic, μ_k, coefficient of friction independent of the velocity v (Fig. 2a). Fig. 2b shows the steady-state version of the Dieterich–Ruina friction law, highlighting the non-monotonic velocity dependence, while Fig. 2c shows the hysteresis effect of the chosen rate-and-state friction law due to the presence of the state variable. The hysteresis takes place during sticking and prolongs its effect within the velocity-weakening regime that occurs at low velocities.

The results for the frictional systems are obtained by means of a numerical integration scheme based on the detection of both stick and slip event conditions and using $ode45$ and $ode23s$ (see also Marino and Cicirello, 2020 for further details). For the sake of clarity, the main steps of the algorithms are illustrated in Appendix, where Algorithm 1 refers to the Amontons–Coulomb case and the steady-state version of the Dieterich–Ruina law, while Algorithm 2 describes the case of using a rate-and-state friction law.

For all cases, a comparative sensitivity analysis is carried out by independently varying each friction model parameter. The comparison is performed within a single period of the cyclic responses, focusing on a time segment contained between two zeros. For the response cycle of reference, different quantities are investigated: time vs. displacement, time vs. velocity and harmonic load vs. displacement response.

2.1. Amontons-Coulomb law

The dimensional equation of motion containing the Amontons–Coulomb law reads as follows:

$$m\ddot{x} + kx + F(v) = P\cos(\omega t) \tag{1}$$

where the origin of the coordinate x refers to the untensioned state of the spring. The friction force is characterized as a function of the slip state ($v \neq 0$) and the stick state in the following way:

$$F(v) = \begin{cases} -\mu_k N \operatorname{sgn}(v) & \text{if } v \neq 0 \\ [-\mu_s N, \mu_s N] & \text{otherwise} \end{cases} \tag{2}$$

in which N identifies the normal load exerted by the sliding mass m on the ground. To allow a comparative study, Eq. (1) is transformed into its non-dimensional form, which reads as

$$r^2\bar{x}'' + \bar{x} + \bar{\mu}(\bar{v}) = \cos\tau \tag{3}$$

where

$$\tau = \omega t \qquad \text{and} \qquad \bar{x} = \frac{x}{P/k} \tag{4}$$

are the dimensionless time and spatial coordinates, respectively, and the operator $(')$ stands for the derivative with respect to τ. The frequency ratio r is the ratio between the excitation and natural frequency of the system, defined as

$$r = \frac{\omega}{\sqrt{k/m}}. \tag{5}$$

The friction force is adimensionalized with respect to the harmonic load amplitude P, complying the same conditions as in Eq. (2)

$$\bar{\mu}(\bar{v}) = \begin{cases} -\bar{\mu}_k \operatorname{sgn}(\bar{v}) & \text{if } \bar{v} \neq 0 \\ [-\bar{\mu}_s, \bar{\mu}_s] & \text{otherwise} \end{cases} \tag{6}$$

where the non-dimensional velocity has been denoted with $\bar{v}$. The static, $\bar{\mu}_s$, and kinetic, $\bar{\mu}_k$, friction ratios are therefore defined as

$$\bar{\mu}_s = \mu_s \frac{N}{P} \qquad \text{and} \qquad \bar{\mu}_k = \mu_k \frac{N}{P}. \tag{7}$$

Note that throughout the paper we indistinguishably refer to Eq. (7) as friction coefficients or friction ratios.

2.1.1. Sensitivity analysis for the Amontons-Coulomb law

Two cases are explored to assess the impact of the static and kinetic friction coefficients variation on the different chosen quantities. For both cases, the simulation results refer to a two-stop stick–slip motion. For the first case, see Fig. 3, a single friction coefficient is assumed such that $\bar{\mu}_s = \bar{\mu}_k$. A frequency ratio $r = 0.3$ was chosen and $\bar{\mu}_k$ was varied between 0.3 and 0.5, with steps of 0.05. By inspecting Fig. 3a,b, it can be deduced that if a single friction coefficient is assumed, its variation has a very moderate influence on the shape of both displacement and velocity responses. In general, it can be observed that for higher kinetic friction ratios, the stick event initiates for a slightly lower absolute displacement of the mass. Fig. 3c relates the dynamic excitation to the dynamic displacements, and as far as the sliding phases concerns, different values of the kinetic friction ratio $\bar{\mu}_k$ tend to enlarge these curves horizontally, while keeping the various sliding traits almost parallel between each other. This is an expected result, since a higher kinetic friction leads to a higher energy dissipation during the sliding phase, which is directly proportional to the area enclosed in the excitation–displacement curves, and to a general increase of the time during which the mass sticks. It is worth underlying that, if the parameter $\bar{\mu}_s = \bar{\mu}_k$ is further increased, the system would eventually get permanently stuck

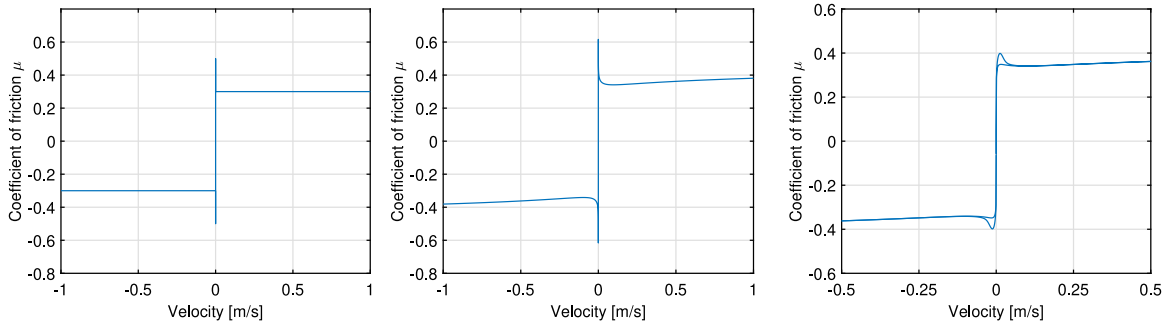

(a) Amontons-Coulomb law (b) Steady-state version of the rate-and-state friction law (c) Rate-and-state friction law

Fig. 2. Qualitative behaviour of the chosen friction laws. Concerning the Dieterich–Ruina friction law, the reference model parameters are indicated in Table 1.

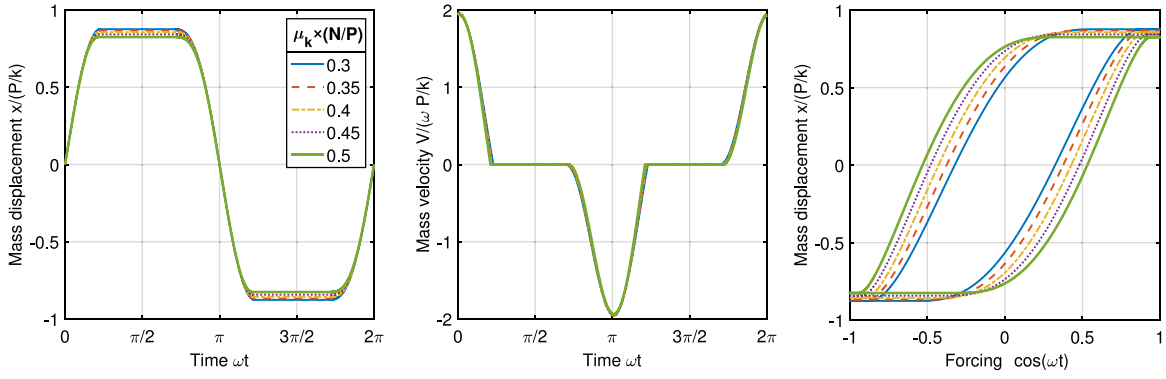

(a) Time vs displacement (b) Time vs velocity (c) Forcing vs displacement

Fig. 3. Cyclic response of a 1-DOF system with Amontons–Coulomb friction for $r = 0.3$, varying $\bar{\mu}_k$ and $\bar{\mu}_s = \bar{\mu}_k$.

when $\bar{\mu}_s = 1$, i.e. when the static friction force equates the amplitude of the harmonic forcing.

Fig. 4 refers to the second case, for which two different coefficients of friction were chosen, such that $\bar{\mu}_s \neq \bar{\mu}_k$. For the displayed simulations, the kinetic friction ratio was kept at 0.4, while the static friction ratio was varied between 0.4 and 0.8. As expected, an increase of the static coefficient leads to an increased spring displacement amplitude since the mass will start slipping at a higher excitation force. This will cause a general increase of the mass velocity, first observed by means of a clockwise rotation and consequent increase of slope of the sliding curve around zero at $\tau = \pi$ in the dynamic displacement vs. time plot (Fig. 4a). The same effect is clearly visible in Fig. 4b where the absolute values of velocities increase with $\bar{\mu}_s$. Concerning the excitation–displacement plot in Fig. 4c, it can be seen that in contrary to the curve expansion shown in Fig. 3c, there is an anti-clockwise rotation around the zero mass displacement of the sliding trait for increasing values of the static friction ratio. Since the kinetic friction is not changing, the corresponding variation of the dissipated energy will not show significant variations.

The role played by varying the static or kinetic friction ratio within the excitation-dynamic response graphs shown in Figs. 3c and 4c, can also be elucidated by inspecting the time lag, or phase difference, generated between the dynamic excitation and the corresponding response, as illustrated in Fig. 5a. The continuous blue and red curves refer to the dynamic displacement obtained by assuming a single coefficient of friction such as $\bar{\mu}_s = \bar{\mu}_k$, being $\bar{\mu}_k$ equal to 0.3 (case 1) and 0.5 (case 2), for the respective curves, while the corresponding excitation is indicated by the dashed lines characterized by $r = 0.3$. Note that while the dynamic responses do not exhibit any significant variation for an increase of $\bar{\mu}_k$, the time-lag between the excitation and the response increases accordingly, due to an increase of dissipation during the sliding phases (traits 6–2 and 3–5 in Fig. 5(a),(b)). To complete the picture, the continuous and dashed green lines in Fig. 5a represent the dynamic displacement and the corresponding excitation for a case in which a difference between $\bar{\mu}_s$ and $\bar{\mu}_k$ is assumed (case 3). To highlight the effect of varying $\bar{\mu}_s$, the value of $\bar{\mu}_k$ was chosen equal to 0.3, therefore comparable to case 1 represented by the blue line, while $\bar{\mu}_s$ is 0.7. Due to the same value of $\bar{\mu}_k$, the time-lag between the dynamic excitation and the corresponding response between case 1 and case 3 remains unaltered, while the presence of a different value of $\bar{\mu}_s$ increases the maximum dynamic displacement during the sticking phase (traits 2–3 and 5–6). The invariance of the time-lag and the increase of the maximum displacement, translates into an anti-clockwise rotation of the sliding traits around the point of zero displacement shown in Fig. 5b.

2.2. Dieterich-Ruina law

A regularized and non-monotonic version of the Dieterich–Ruina model (Dieterich, 1979; Ruina, 1983) is used, which defines μ as a dependent variable by the following relation

$$\mu(v,\theta) = \mu_* + a \ln\left(\frac{v}{V_*}\right) + b \ln\left(c + \frac{\theta}{\theta_*}\right) \tag{8}$$

where v is the sliding velocity of the mass, θ is an internal state variable, the subscript "$*$" defines steady-state reference values of μ and θ for a chosen sliding velocity V_*, a and b are dimensionless model parameters. The introduction of the parameter c was originally proposed in Putelat et al. (2007) and subsequently tested against experimental results in Cabboi et al. (2016). Such parameter confers a residual strength to the friction force at high sliding velocities, during which the state variable θ, that governs the interfacial state behaviour, is supposed to have no influence on the friction force. Therefore, the consequence

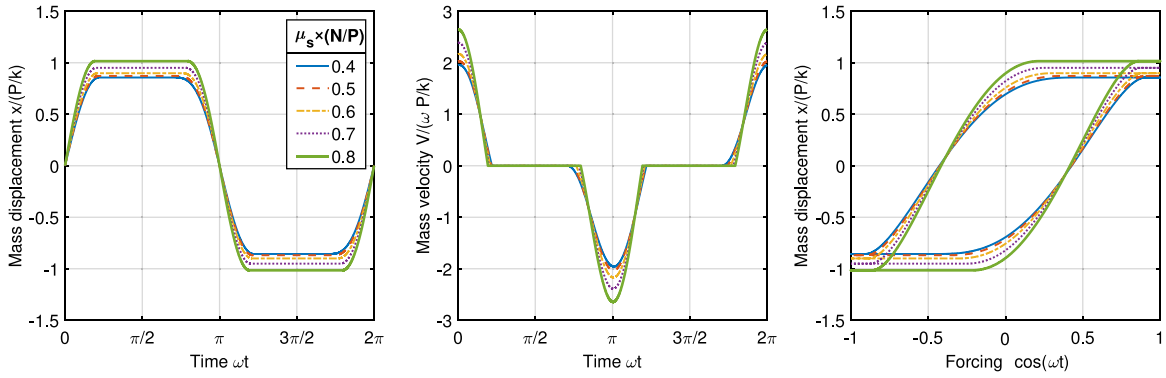

(a) Time vs displacement (b) Time vs velocity (c) Forcing vs displacement

Fig. 4. Cyclic response of a 1-DOF system with Amontons–Coulomb friction for $r = 0.3$, $\bar{\mu}_k = 0.4$ and varying $\bar{\mu}_s$.

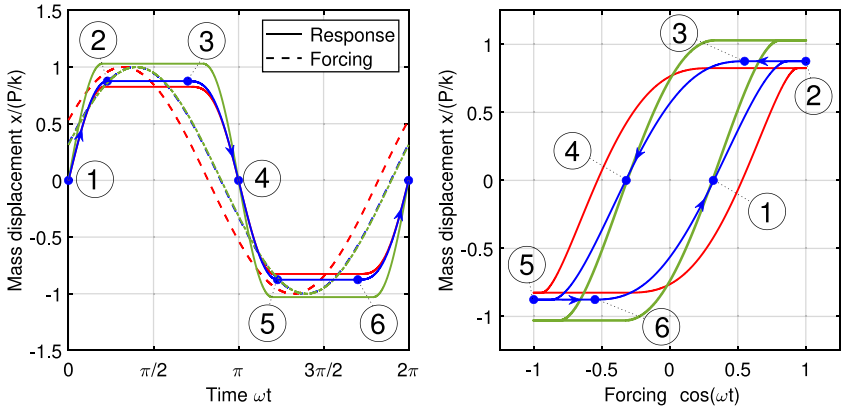

(a) Time vs displacement (b) Forcing vs displacement

Fig. 5. (a) Dynamic displacement vs. time graphs. The continuous lines define the dynamic displacement response, with the following system parameters: blue line $r = 0.3$, $\bar{\mu}_k = \bar{\mu}_s = 0.3$ (case 1); red line $r = 0.3$, $\bar{\mu}_k = \bar{\mu}_s = 0.5$ (case 2); green line $r = 0.3$, $\bar{\mu}_k = 0.3$, $\bar{\mu}_s = 0.7$ (case 3). The dashed lines indicate the corresponding dynamic excitation; (b) Corresponding excitation vs dynamic displacement graphs. (For interpretation of the references to colour in this figure legend, the reader is referred to the web version of this article.)

of introducing c is to generate two friction force regimes, as shown in Fig. 2b: a velocity-weakening regime, during which the slope of the friction–velocity curve is negative and a velocity-strengthening regime, during which the coefficient of friction increases with velocity. The need of such non-monotonic curve agrees well with experimental findings for various material combinations illustrated in Bureau et al. (2002), Cabboi et al. (2016), Heslot et al. (1994), Weeks (1993) and Shroff and de Boer (2016).

To complete Eq. (8), the state variable θ needs an evolutionary law given by the standard Dieterich ageing law (Dieterich, 1979) that reads as follows

$$\frac{\mathrm{d}\theta}{\mathrm{d}t} = 1 - \frac{|v|\theta}{L} \tag{9}$$

where the parameter L is a length-scale parameter characterizing an observed transient behaviour in velocity jump and slide-hold-slide friction tests (Marone, 1998). In the numerator of Eq. (9), the absolute value is used to preserve the ageing law for negative values of the sliding velocity. As mentioned earlier, the ageing law defined by Eq. (9) was added to reproduce a transient relaxation phenomenon that characterizes the friction force if subject to a sudden sliding velocity jump, from v_1 to v_2 (in which v_2 tends to be an order of magnitude higher or smaller than v_1, see Marone (1998) for further details and the annotated Fig. 6a for a graphical illustration of the transient phenomenon). The friction force is assumed to be in a steady-state condition ($\mathrm{d}\theta/\mathrm{d}t = 0$) at the two reference sliding velocities v_1 and v_2.

The effect of the state variable on the friction force, can also be visualized by applying a small oscillatory perturbation $\tilde{v}(t)$ around a chosen sliding velocity v, where $\tilde{v}(t) \ll v$. This line of reasoning was illustrated in three previous studies (Cabboi et al., 2016; Cabboi and Woodhouse, 2018, 2020), leading to a linearized version of the rate-and-state friction law around an arbitrary sliding velocity. By taking the Fourier transform of the linearized friction law, it is possible to formulate an expression of a frictional frequency response function $\beta(\omega)$. Such function represents the slope of the friction curve around an arbitrary chosen sliding velocity, and due to the presence of the state variable it is a complex number. The derivation of the expression of $\beta(\omega)$ for the chosen friction law, Eq. (8), can be found in Cabboi et al. (2016), and the final expression reads as follows

$$\beta(\omega) = \frac{\tilde{\mu}(\omega)N}{\tilde{v}(\omega)} = N\frac{(\mu_{ss,v} + \omega^2 t_\theta^2 \mu_v) + \mathrm{i}\omega t_\theta(\mu_v - \mu_{ss,v})}{1 + \omega^2 t_\theta^2} \tag{10}$$

where i is the imaginary number defined as $\mathrm{i}^2 = -1$, $\tilde{\mu}$ represents the linearized term of the friction force expression. Parameters μ_v and $\mu_{ss,v}$ are partial derivatives of the rate-and-state law with respect to velocity, note that the subscript "ss" stands for the steady-state version of the rate-and-state friction law that will be described later. Parameter t_θ defines the inverse of the partial derivative of the state evolution law with respect to θ. By assuming the Dieterich–Ruina law as a realization of the rate-and-state expression, the partial derivatives read as follows (see also Cabboi et al. (2016) for further details)

$$\mu_{ss,v} = \frac{a}{v} - \frac{bV_*}{v(V_* + vc)}; \quad \mu_v = \frac{a}{v}; \quad t_\theta = \frac{L}{v}. \tag{11}$$

It is important to note that Eq. (10) differs by an initial minus sign from the expression shown in Eq. (30) in Cabboi et al. (2016). The minus sign

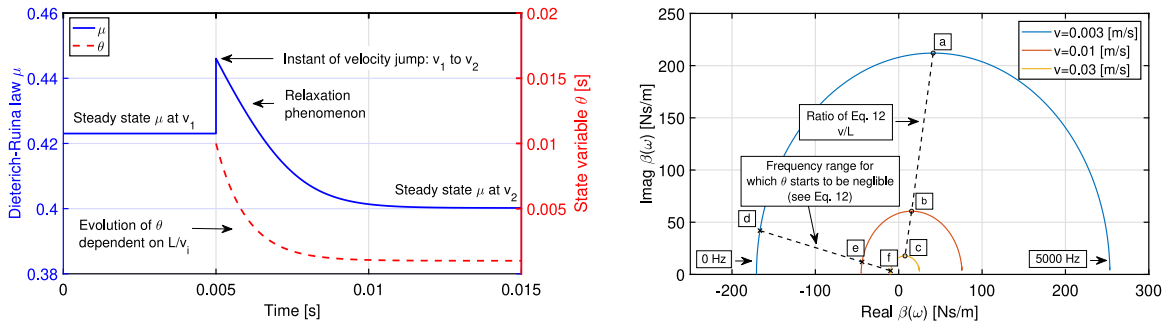

(a) Speed jump simulation

(b) Frequency response of dynamic friction $\beta(\omega)$

Fig. 6. (a) Dieterich–Ruina law applied to a sliding velocity jump from v_1 (0.1 mm/s) to v_2 (1 mm/s). The model parameters for this example are: $a = 0.01$, $b = 0.02$, $V_* = 1$ mm/s, $L = 1e{-}6$ m, $c = 0.01$ and $\epsilon = 0$; (b) Frequency response of dynamic friction, $\beta(\omega)$. The model parameters for Eq. (10) are listed in Table 1, and an arbitrary normal load of 10 N was assumed. The frequency range spans between 0 and 5 kHz, and three different velocities v were chosen: 0.003 m/s (blue line), 0.01 m/s (red line) and 0.03 m/s yellow line. Markers (a), (b) and (c) refer to frequency values of 47, 159 and 477 Hz, respectively, while markers (d), (e) and (f) are chosen to be 10 times lower then the previous ones. (For interpretation of the references to colour in this figure legend, the reader is referred to the web version of this article.)

was needed to fit the sign convention of the measured forces during the experiments described in Cabboi et al. (2016). The expression of $\beta(\omega)$ is visualized in Fig. 6b for increasing values of velocities (0.003–0.01–0.03 [m/s]) and for a frequency range between 0–5 kHz. The values of reference for the Dieterich–Ruina law are indicated in Table 1. Fig. 6b highlights that the $\beta(\omega)$ curves tend to shrink for increasing values of sliding velocities. At zero frequency, regardless of the velocity, Eq. (10) simplifies into the $\mu_{ss,v}$, representing the slope of the steady-state version of the Dieterich–Ruina law. For frequencies higher than zero, it can be observed that the initial segment of the $\beta(\omega)$ curves shows a negligible dependence between frequency and real part and the imaginary part has a lower amplitude compared to the real part. This region encapsulates the forcing condition for which the state variable can be neglected. To better quantify this region, we may seek for conditions to reduce the imaginary part of Eq. (10) to zero. For a finite difference between $\mu_v - \mu_{ss,v}$, it can be deduced that in order to decrease the imaginary part, there is an interplay between two time-scales defined by the product ωt_θ. An eventual decrease of such product allows the imaginary component to vanish. In general, the following inequality between the time-scale of the forcing defined by ω and the time-scale of the interfacial asperity dynamics represented by t_θ, characterizes the condition for which the state variable becomes negligible during a perturbed sliding regime

$$\omega \ll \frac{v}{L}. \tag{12}$$

Eq. (12) suggests that for a fixed ω, any kinetic (or rate-dependent) friction law would be justified provided the ratio between sliding velocity and asperity-related length-scale is high enough. Note that a similar condition was already proposed in a previous work, see Elmer (1997), independently of the assumed rate-and-state friction law. The ratio v/L is highlighted in Fig. 6b through circled markers (see points (a), (b) and (c)), while a threshold region defined by frequencies 10 times lower than the v/L values, start to define the area in which the effect of the state variable on sliding can be neglected.

Besides the described effects on a perturbed sliding regime, be it through a velocity jump or by means of a small oscillatory perturbation, the assumed state evolution law (ageing law) exhibits the most predominant effect during a sticking regime when $v = 0$. As it can be deduced by Eq. (9), during a stationary contact the parameter θ increases linearly with time. The latter property is often called as time-dependent healing (Dieterich, 1979; Bureau et al., 2002; Marone, 1998). However, the Dieterich–Ruina law cannot be straightforwardly used for the case of stationary contact, since the functional form of Eq. (8) still poses a problem in case of zero velocity due to the first logarithmic dependence on velocity. A regularization was proposed in Rice and Ben-Zion (1996) and Putelat et al. (2007), forcing the coefficient of friction to rapidly decrease towards zero as soon as the velocity approaches the zero value. However, the physical justification of such a rapid and steep decrease of the friction coefficient within a friction vs. velocity graph is highly questionable. To eliminate such singularity, we propose a simpler approach, by introducing a small parameter ϵ ($\epsilon \ll 1$) that acts as a cut-off or residual velocity, allowing a realization of the static coefficient of friction at $v = 0$. The regularized expression of the friction coefficient reads as

$$\mu(v,\theta) = \mu_* + a \ln\left(\frac{|v|+\epsilon}{V_*}\right) + b \ln\left(c + \frac{\theta}{\theta_*}\right). \tag{13}$$

Therefore, according to Eq. (13), during a stationary contact ($v = 0$) an increase of θ results in a logarithmic increase of the static friction coefficient, described by

$$\mu_s(\theta_0, \Delta t) = \mu_* + a \ln\left(\frac{\epsilon}{V_*}\right) + b \ln\left(c + \frac{\theta_0 + \Delta t}{\theta_*}\right) \quad \text{where} \quad \theta_* = \frac{L}{V_*} \tag{14}$$

and $\Delta t = t - t_0$, being t_0 and θ_0 the initial time instant and internal state, respectively, at the onset of the sticking phase. Based on Eq. (14), it can be deduced that the increase of the static friction coefficient during a stationary contact is directly proportional to the weighting factor b and to the value of L, a characteristic property of the surfaces in contact.

For the comparative analysis of this study, a steady-state version of the rate-and-state friction law was also used. A steady-state of the dynamic friction law implies that $\mathrm{d}\theta/\mathrm{d}t \approx 0$. Under this condition, parameters L and θ can be neglected within the Dieterich–Ruina law. By imposing the latter condition on Eq. (9), we deduce that

$$\frac{\mathrm{d}\theta}{\mathrm{d}t} = 1 - \frac{|v|\theta}{L} = 0 \qquad \rightarrow \qquad \theta_{ss} = \frac{L}{|v|} \approx \theta_{ss} = \frac{L}{|v|+\epsilon}. \tag{15}$$

It is worth noting that the parameter ϵ is introduced also in this equation in order to eliminate the singularity in the steady-state expression of the Dieterich–Ruina law. Taking into account the expressions for θ_{ss} and θ_*, we can eliminate parameters L and θ from the friction law, obtaining the following relation

$$\mu(v) = \mu_* + a \ln\left(\frac{|v|+\epsilon}{V_*}\right) + b \ln\left(c + \frac{V_*}{|v|+\epsilon}\right). \tag{16}$$

Eq. (16) enables us to make few considerations concerning the behaviour of the friction force–velocity relation. The non-monotonicity of Eq. (16) implies the presence of a minimum velocity, that marks the transition point between the velocity-weakening and the velocity strengthening regime, and is given by

$$v_{min} \approx \frac{V_*}{c} \times \frac{(b-a)}{a} \tag{17}$$

for which the parameters containing ϵ were neglected (since assumed to be very small, $\epsilon \ll 1$). Eq. (17) was derived by taking the partial derivative of Eq. (16) with respect to the sliding velocity v, and setting

the zero condition for such derivative. Positive values of v_{min} are provided only if the term $(b-a)$ is positive.

As mentioned before, the introduction of ϵ, enables the quantification of a possible value of the static coefficient of friction as soon as v tends to zero. Setting v to zero in Eq. (16), the expression of the static coefficient of friction is defined as

$$\mu_s = \mu_* + a \ln\left(\frac{\epsilon}{V_*}\right) + b \ln\left(c + \frac{V_*}{\epsilon}\right). \tag{18}$$

Eq. (18) can be reduced to a simpler form. Given that $\epsilon \ll 1$, and provided that $\epsilon \ll V_*$, the ratio V_*/ϵ contained in the second parenthesis becomes dominant, leading to the following approximate expression

$$\mu_s \approx \mu_* - (b-a) \ln\left(\frac{\epsilon}{V_*}\right) \tag{19}$$

Since ϵ can be assumed always smaller than V_*, Eq. (19) ensures that $\mu_s > \mu_*$ for positive values of $(b-a)$. The expression of the static friction coefficient will later be used to provide initial guesses for the optimization runs illustrated in Section 3. With reference to the optimization, it is worth mentioning that negative values of $\mu(v)$ need to be avoided. Since specific combinations of model parameters may generate negative values of the friction coefficients estimated by the Dieterich–Ruina law, only the model parameters that comply the following inequality of $\mu(v_{min})$ are investigated:

$$\mu(v_{min}) \approx \mu_* + a \ln\left(\frac{b-a}{ca}\right) + b \ln\left(\frac{cb}{b-a}\right) > 0. \tag{20}$$

So far, we used the Dieterich–Ruina law as a possible realization of a rate-and-state friction law able to quantify the dependence of the coefficient of friction on variables such as the sliding velocity and an internal state variable. To define a friction force F (as depicted in Fig. 2), in the original formulation (see Dieterich, 1979), the Amontons–Coulomb proportionality between the normal force and the friction force was used. For the sake of simplicity, the same proportionality was assumed in this study to define the friction force. It is worth mentioning that a non-trivial dependence on the normal load will inevitably call for an extra state variable as suggested in previous studies (Linker and Dieterich, 1992; Prakash, 1998; Tal et al., 2020), leading to a 2-DOF system with a bi-directional friction law, which investigation falls outside the scope of this study.

To summarize the assumed laws in this section and following the nondimensionalization adopted in Section 2.1, the adimensionalized equations for the steady-state version of the friction force F formulated by means of the Dieterich–Ruina law, that leads to a rate-dependent model, reads as

$$\bar{\mu}(\bar{v}) = \begin{cases} -\left[\bar{\mu}_* + \bar{a} \ln\left(\frac{|\bar{v}|+\bar{\epsilon}}{\bar{V}_*}\right) + \bar{b} \ln\left(c + \frac{\bar{V}_*}{|\bar{v}|+\bar{\epsilon}}\right)\right] \operatorname{sgn}(\bar{v}) & \text{if } \bar{v} \neq 0 \\ [-\bar{\mu}_s, \bar{\mu}_s] & \text{otherwise} \end{cases} \tag{21}$$

while the adimensionalized expressions of the friction force F following the rate-and-state law are defined by

$$\bar{\mu}(\bar{v}, \bar{\theta}) = \begin{cases} -\left[\bar{\mu}_* + \bar{a} \ln\left(\frac{|\bar{v}|+\bar{\epsilon}}{\bar{V}_*}\right) + \bar{b} \ln\left(c + \frac{\bar{\theta}\bar{V}_*}{\bar{L}}\right)\right] \operatorname{sgn}(\bar{v}) \quad \text{and} \\ \quad \frac{\mathrm{d}\bar{\theta}}{\mathrm{d}\tau} = 1 - \frac{|\bar{v}|\bar{\theta}}{\bar{L}} & \text{if } \bar{v} \neq 0 \\ [-\bar{\mu}_s(\bar{\theta}_0, \Delta\tau), \bar{\mu}_s(\bar{\theta}_0, \Delta\tau)] & \text{otherwise} \end{cases} \tag{22}$$

where:

$$\bar{a} = a\frac{N}{P}, \qquad \bar{b} = b\frac{N}{P}, \qquad \bar{V}_* = \frac{V_*}{\omega P/k}, \qquad \bar{\epsilon} = \frac{\epsilon}{\omega P/k}, \qquad \bar{\theta} = \omega\theta$$
$$\text{and} \qquad \bar{L} = \frac{L}{P/k}. \tag{23}$$

The adimensionalization also enables us to further simplify the condition formulated in Eq. (12) into

$$\bar{L} \ll \bar{v}. \tag{24}$$

Eq. (24) is independent of the forcing frequency, and suggests that for high sliding velocities, the state variable can be neglected. This was qualitatively deduced by inspecting the general decrease of the $\beta(\omega)$ curves for increasing values of sliding velocities.

2.2.1. Sensitivity analysis for the Dieterich-Ruina law

Ranges and reference values for the Dieterich–Ruina friction model parameters were assumed and listed in Table 1. The values of a, b and L are indicatively taken from previous studies (Cabboi et al., 2016; Cabboi and Woodhouse, 2018) showing ranges of fitted rate-and-state model parameters for different material combinations (e.g. polymer-glass, polymer-steel), while c, μ_*, V_* and ϵ were chosen in order to mimic friction curves that could most likely match a realistic friction force dependence with velocity. The same ranges and values were also used for their corresponding parameterized versions, $\bar{a}$, $\bar{b}$, $\bar{L}$, $\bar{V}_*$, $\bar{\mu}_*$ and $\bar{\epsilon}_*$. The latter ones were adopted for the sensitivity study concerning the cyclic response and the optimization process described in Section 3. Constant parameters are also listed in Table 1 as reference values. Before assessing the influence of each model parameter on the dynamic response of the 1-DOF oscillator, it is worth highlighting the role each model parameter plays for the prediction of the friction coefficient–velocity curve. Parameters a, b, L, c, μ_* and ϵ were varied separately within the ranges indicated in Table 1, while reference values were chosen for the fixed parameters. For almost all the above mentioned model parameters, Eq. (16) was used to highlight their sensitivity on the Dieterich–Ruina law, while for parameter L the complete rate-and-state law was adopted (see Eqs. (9) and (13)).

The influence of parameter L on the friction curve is shown in Fig. 7a. Eqs. (9) and (13) were used in combination with an assumed sinusoidal varying velocity between −1 and 1 m/s, and a frequency ω of 10 rad/s. For the simulated continuous sliding motion, the acceleration (upper line) and deceleration traits (lower line) for positive velocities are shown for each curve. The main effects of the state variable is to generate a slight shift of the maximum value of the coefficient of friction at low velocities, that occurs at a $v \neq 0$, and to induce an hysteresis behaviour, leading to lower values of the coefficient of friction for the deceleration traits with respect to the acceleration part. It can be deduced from Eq. (12), that for a fixed ω, a decrease of L may allow to neglect the state variable for a larger velocity range. This outcome can be observed by comparing the dash-dotted yellow curve and the continuous blue line in Fig. 7a, generated for a low and a high value of L, respectively. The yellow curve highlights an influence of the state variable within the mm/s domain of velocity, while its effect ceases for higher velocities, during which the acceleration and deceleration traits perfectly overlap. Lower values of L (for instance 0.001 m), tend to prolong the effect of the state variable within the cm/s velocity domain. For further simulations, L was kept fixed at 10^{-5} m. It is worth clarifying that the friction reduction effect at low velocities, visible in Fig. 7a, is due to the logarithm argument $(c+\theta/\theta_*)$ in Eq. (13) that tends to be lower than 1, depending on the ratio defined by θ_* and on the evolution of θ. Note that in case of stick–slip motion, the time spent in stationary contact during the stick regime allows an increase of θ, which leads to an increase of the static friction coefficient; therefore, a friction reduction of the type shown in Fig. 7a will be hard to observe.

As described earlier, the Dieterich–Ruina law was modified for the case of velocities approaching zero values. The introduction of the parameter ϵ enables an estimation of the static coefficient of friction. Fig. 7b shows the influence of the parameter ϵ on the friction–velocity curves obtained with Eq. (16). The choice of ϵ has a direct effect limited to the value of the static friction coefficient and to the friction coefficients close to the zero velocity point, whereas no relevance of ϵ

Table 1
Chosen ranges and reference values for the Dieterich–Ruina law. The ranges and reference values were taken from previous studies (Cabboi et al., 2016; Cabboi and Woodhouse, 2018).

Parameters	a	b	L [m]	c	V_* [m/s]	μ_*	ϵ
Reference values	0.038	0.065	10^{-5}	0.022	0.003	0.4	10^{-6}
Range	0.01–0.09	0.01–0.16	10^{-3}–10^{-7}	0.01–0.1	–	0.3–0.5	10^{-4}–10^{-8}

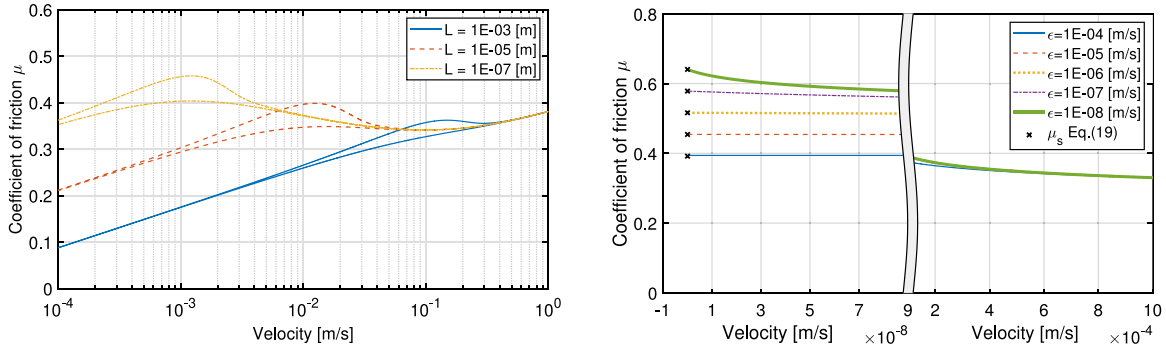

(a) Variation of L (b) Variation of ϵ

Fig. 7. (a) Rate-and-state version of the Dieterich–Ruina law, (see Eqs. (13) and (9)), for a case of continuous sliding motion characterized by a maximum velocity of 1 m/s and a frequency ω of 10 rad/s; (b) Steady-state version of the Dieterich–Ruina law. The static coefficient of friction, μ_s was estimated by Eq. (19) and is defined by a black cross in graph (b). Note that graph (b) was truncated along the x-axis, highlighting two different regimes of sliding velocity at a smaller and higher order of magnitude. (For interpretation of the references to colour in this figure legend, the reader is referred to the web version of this article.)

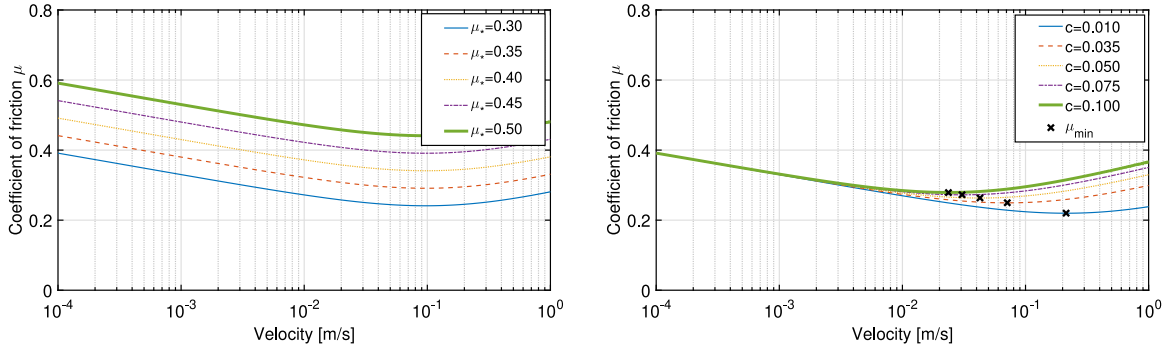

(a) Variation of μ_* (b) Variation of c

Fig. 8. Steady-state version of the Dieterich–Ruina law for the case of continuous sliding motion for varying values of: (a) μ_* and (b) c. Ranges and reference values are listed in Table 1.

was detected for velocities higher than zero, as displayed by the right part of Fig. 7b. The values of the static coefficients were also estimated by means of the approximated Eq. (19), defined by a black cross in Fig. 7b, showing an excellent match with the starting point of the friction–velocity curves. For the upcoming analysis, ϵ was kept fixed at 10^{-6} m/s.

Fig. 8a shows five different curves obtained by varying μ_*. The effect of such parameter, linked to the chosen sliding velocity V_*, consists in translating the curve upwards or downwards for increasing or decreasing values of μ_*, respectively. If compared to the Amontons–Coulomb law, this would reflect to a change of μ_k and μ_s. The effect of parameter c is displayed in Fig. 8b and can be also be appreciated by inspecting Eq. (17). An increase of c leads to higher value of the minimum transition velocity, v_{min}, and to a corresponding decreasing value of μ_{min} marked by a black cross in Fig. 8b. Note that parameter c could be used to match the Stribeck effect typically observed in sliding friction experiments. In fact, smaller values of c lead to a shift of the minimum of the friction curves towards higher velocities, thus extending the velocity range where the velocity-weakening takes place. Moreover, when small values of c are assumed, the branch of the friction curve following this minimum presents a low dependence on the velocity, therefore also resembling an Amontons–Coulomb law characterized by different static and kinetic friction coefficients.

Fig. 9 shows the influence of parameter a and b on the friction curve. Note that as soon a is higher than b (see the purple (a = 0.07) and green (a = 0.09) curve in Fig. 9a and the continuous blue curve (b = 0.01) in Fig. 9b), the friction curve exhibits a monotonic increasing trend starting from μ_s. A monotonic increase of such kind is counter-intuitive, however it is worth highlighting that experimental evidence do exist highlighting the non-reversibility of the friction force–velocity curve relation, in which the deceleration traits exhibit kinetic friction coefficients higher than the static ones (Wiercigroch et al., 1999; Wojewoda et al., 2008; Saha et al., 2016). In the current study, we assumed a perfect reversibility of the steady-state version of friction force - velocity curve. Eq. (17) also suggests that for a positive transition velocity to exist, $(b-a)$ has to be positive. This condition will be enforced for the optimization runs in Section 3. For completeness, it is worth adding that the above described increasing trend of the friction coefficient estimated by means of a steady-state version of the Dieterich–Ruina law, can still occur for low positive values of $(b-a)$ combined with high values of a. Such parameter space was eventually kept within the optimization runs described in Section 3.

Overall, the variation of a and b exhibited the most significant changes for the friction curve: it affects both the velocity-weakening and strengthening sliding regimes and the position of the minimum

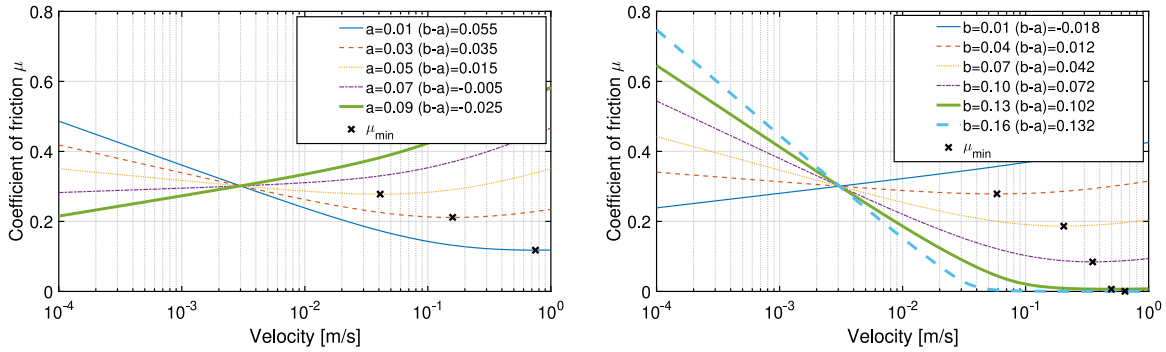

(a) Variation of a (b) Variation b

Fig. 9. Steady-state version of the Dieterich–Ruina law for the case of continuous sliding motion for varying values of: (a) a and (b) b. Ranges and reference values are listed in Table 1. (For interpretation of the references to colour in this figure legend, the reader is referred to the web version of this article.)

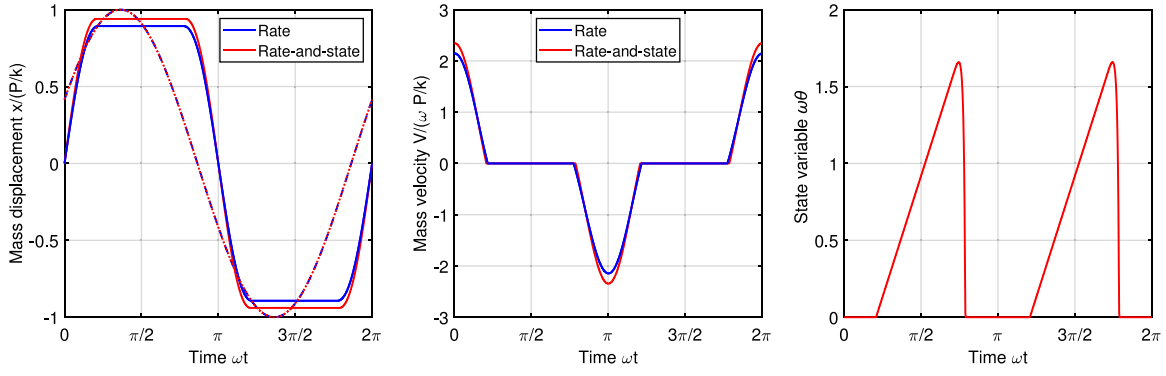

(a) Time vs displacement (b) Time vs velocity (c) Time vs state variable

Fig. 10. Comparison between the cyclic responses of a 1-DOF system with rate-dependent (blue lines) and rate-and-state (red lines) friction for $r = 0.3$. In (a), the dashed lines indicate the corresponding dynamic excitation. Reference values for the simulations are listed in Table 1. (For interpretation of the references to colour in this figure legend, the reader is referred to the web version of this article.)

transition velocity. In combination with parameter c, these model parameters enable to fit an eventual Stribeck effect observed during sliding friction tests. In addition, parameters a and b also allow to tune the static friction coefficient. With reference to the latter observation, an increase of positive values for $(b - a)$, leads to a slight increase of the static friction coefficient and a decrease of the friction coefficients for velocities higher than zero, minimizing the velocity dependency of the friction curve for velocities nearby and higher than v_{min}.

Similarly to what shown in Section 2.1.1, the sensitivity analysis to assess the influence of the Dieterich–Ruina law on the chosen quantities is performed for a two-stop motion. The analysis is carried out by first assessing the influence of the rate-and-state friction law on the cyclic two-stop motion, followed by runs in which the steady-state version of the Dieterich–Ruina law is used. To facilitate the comparison with the results presented in Section 2.1.1, the non-dimensional equations presented in Eqs. (21) and (22) were adopted.

The results presented in Fig. 10 showcase the influence of the state variable during a two-stop motion, for which a frequency ratio of $r = 0.3$ was used. As mentioned in Section 2.2, see Eq. (14), the presence of the state variable leads to an increase of the static coefficient of friction. Such increase is clearly visible in Fig. 10a–b, where the red curve refers to the rate-and-state friction law, while the blue curve depicts the steady-state version of the Dieterich–Ruina law. In fact, it can be observed that the rate-and-state responses are characterized by larger absolute displacements during the sticking phases and slightly higher velocities during the sliding phases. As explained in Section 2.1.1 and shown in Figs. 4a and 5a, these effects are consistent with an increase of the static friction coefficient. Moreover, it can be noted that the transition from sticking to sliding is slightly delayed and smoother when the variation of θ is accounted for. This can be explained by looking at Fig. 10c, where the evolution of the state variable during the two-stop motion is displayed, highlighting a significant difference between the values assumed by θ during sliding and sticking. The stationary contact is characterized by a linear increase of θ, while at the onset of sliding θ tends to rapidly decrease. It is precisely the latter short time interval, during which θ still exhibits high values and while the velocity starts to gradually build up, that leads to the slight shift of the maximum coefficient of friction observed at low velocities, already shown in Fig. 7a. The same shift can also be observed by inspecting the red curve in Fig. 11a, representing the rate-and-state dependent friction force recorded during an arbitrary cycle of a two-stop motion. At low velocities, the presence of the state variable causes a clear separation between the acceleration and deceleration phases during stick–slip, while for the rate-dependent friction force both phases perfectly overlap. However, differently from the friction curves shown Fig. 7a, which have been obtained by using a sinusoidal varying velocity, the red curve in Fig. 11a also exhibits different values of the friction force at $\bar{v} = 0$ for the acceleration and deceleration traits; this is clearly due to the already mentioned increase of the static friction coefficient during the sticking phases. Figs. 11b–c highlight the evolution in time of both recorded friction forces. In Fig. 11b, it can be observed that during the sliding phase, the underlining friction force is always symmetric and the static coefficient of friction at the onset of sticking and sliding remains constant. On the contrary, the rate-and-state dependent friction force during sliding loses its symmetry (see Fig. 11c), showing higher values during the initial acceleration phase at the onset of sliding and lower values at the onset of sticking. The dashed red lines in Fig. 11c represent the logarithmic increase of the static friction force during the sticking phase.

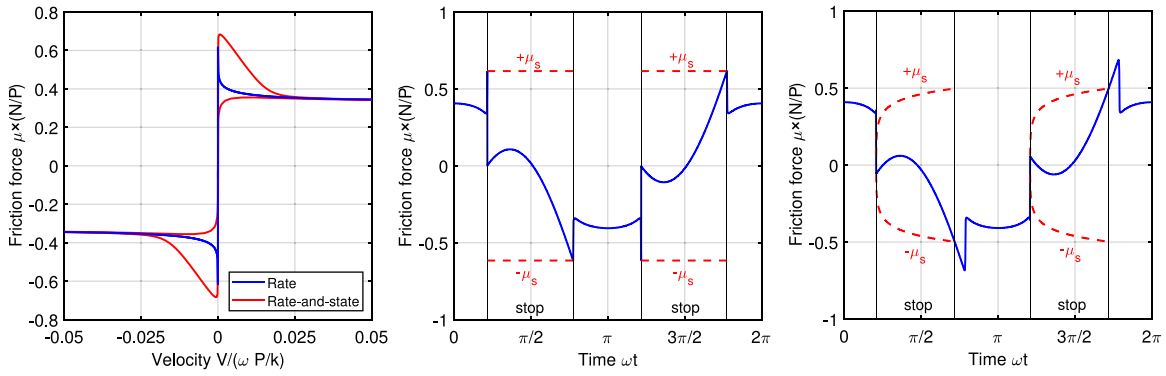

(a) Velocity vs friction force (b) Time vs friction force (rate) (c) Time vs friction force (rate-and-state)

Fig. 11. Comparison between the rate-dependent and rate-and-state dependent friction forces for the 1-DOF system, recorded during a cyclic motion. In (b) and (c), the red curves represent the evolution of the static friction force during the sticking phases. (For interpretation of the references to colour in this figure legend, the reader is referred to the web version of this article.)

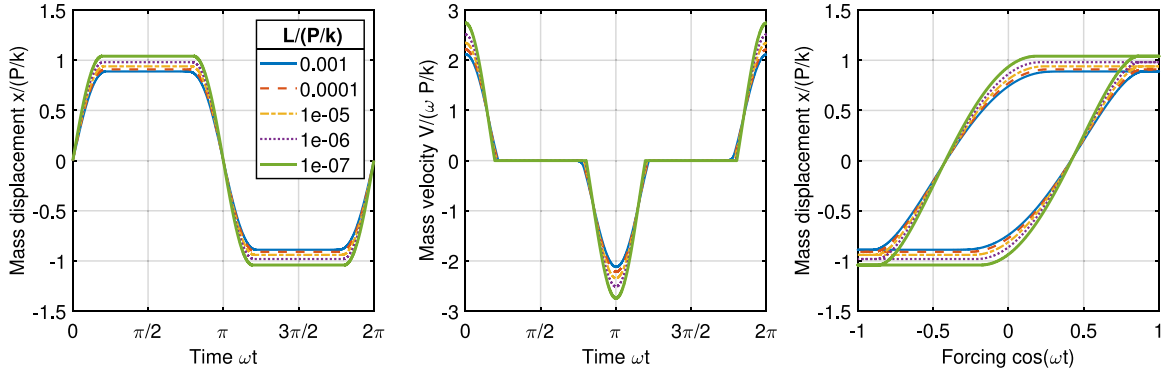

(a) Time vs displacement (b) Time vs velocity (c) Forcing vs displacement

Fig. 12. Cyclic stick–slip response of a 1-DOF system with rate-and-state friction for $r = 0.3$ and varying $\bar{L}$. Reference values are listed in Table 1.

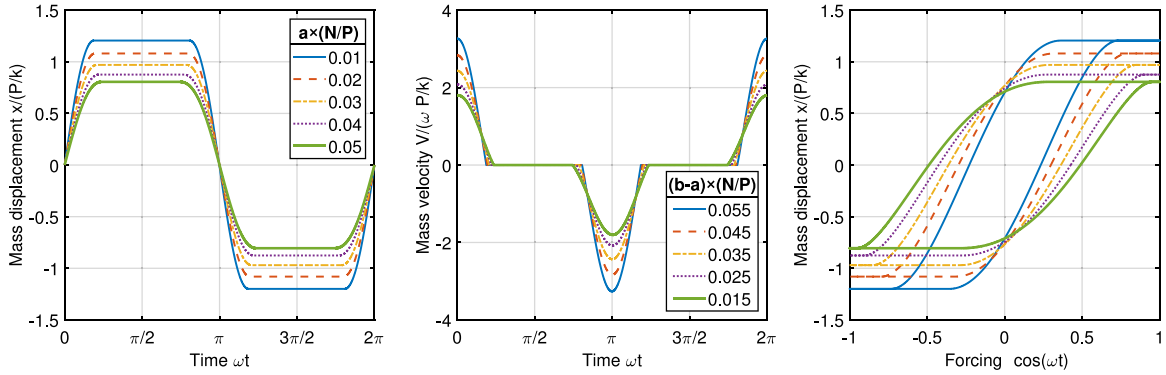

(a) Time vs displacement (b) Time vs velocity (c) Forcing vs displacement

Fig. 13. Two-stop motion of a 1-DOF system with a rate-dependent friction law for $r = 0.3$ and varying a. Reference values are listed in Table 1.

The influence of a varying model parameter $\bar{L}$ during an arbitrary cycle of stick–slip is shown in Fig. 12. As already shown in Fig. 7, low values of $\bar{L}$ tend to reduce the friction force at low velocities, and this reflects into lower displacement values and shorter sticking phases (see Fig. 12a), resulting therefore in lower velocities (see Fig. 12b). Since the effect of parameter $\bar{L}$ is more pronounced at velocities approaching zero, the hysteresis curves in Fig. 12c seem to mimic the excitation vs displacement graphs shown in Fig. 4, where the static friction coefficient of the Amontons–Coulomb law was varied.

To assess the effect of parameters $\bar{a}$ and $\bar{b}$ on the investigated response features, the steady-state version of the Dieterich–Ruina law was used, with a frequency ratio $r = 0.3$. While varying parameters $\bar{a}$ and $\bar{b}$, the condition $(\bar{b} - \bar{a}) \geq 0$ was complied. Figs. 13 and 14 display the same set of figures shown in Fig. 3, highlighting the variation of the displacement and velocity in time, subfigures (a,b), combined with the excitation vs displacement graph, subfigures (c), caused by a varying value of $\bar{a}$ and $\bar{b}$. The variation of parameters $\bar{a}$ and $\bar{b}$, tend to reproduce what has been observed for assuming two different coefficients of friction: a static and kinetic one, see Fig. 4a,b. To facilitate the interpretation of the induced effect of the model parameters $\bar{a}$ and $\bar{b}$, it can be noted that for increasing values of the term $(\bar{b} - \bar{a})$, as shown in Figs. 13b and 14b, there is an increase of the displacement and velocity amplitude. This resemblance with the case of two distinct coefficients of friction can be expected, since the Dieterich–Ruina law

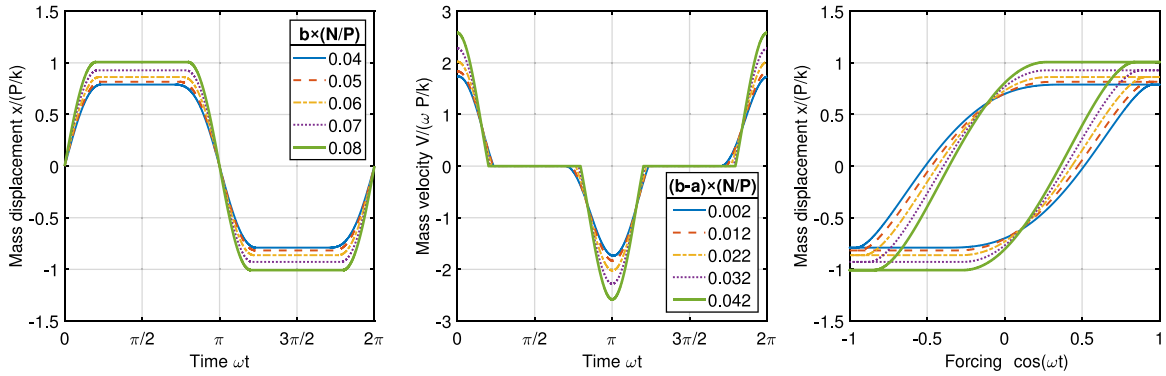

(a) Time vs displacement (b) Time vs velocity (c) Forcing vs displacement

Fig. 14. Two-stop motion of a 1-DOF system with a rate-dependent friction law for $r = 0.3$ and varying b. Reference values are listed in Table 1.

regularizes the sudden drop between a static and kinetic coefficient of friction. In addition, as shown in Fig. 9, a larger difference between $(\bar{b}-\bar{a})$ implies a more significant difference between a static coefficient of friction and the friction coefficients for velocities different than zero. If the condition $(\bar{b}-\bar{a}) \geq 0$ is complied, an increase of $(\bar{b}-\bar{a})$ leads to a general decrease of the friction coefficients for velocities different than zero and a slight increase of the static coefficient of friction. It is the latter increase that leads to an increase of maximum displacements and velocities during the sticking and sliding phases, respectively. The main differences with the cases for which the Amontons–Coulomb static and/or kinetic coefficients of friction were adopted, are illustrated in Figs. 13c and 14c, where the relation between the dynamic response and the excitation is shown. Both dynamic forcing–displacement graphs highlight a somewhat similar pattern as observed in Fig. 4c, where an increase of the static friction ratio led to an anti-clockwise rotation around the zero mass displacement of the sliding trait. Figs. 13c and 14c, seem to reproduce a comparable anti-clockwise rotation by increasing $(\bar{b}-\bar{a})$, that translates to an increase of the static coefficient of friction, as shown in Eq. (19). However, the point around the rotation occurs differs from what observed in Fig. 4c due to the fact that a change of $(\bar{b}-\bar{a})$ not only affects the static friction coefficient but also the relation between the kinetic friction coefficient and the sliding velocity. This observed feature seems to be traceable to the velocity dependence of the friction force.

3. Comparative study between the Amontons-Coulomb and Dieterich-Ruina friction laws

3.1. Optimization procedure

As discussed in the introduction, current friction models are application dependent, meaning that one friction model identified from a specific test setup or validated for a defined application, may not be suitable for an application in which the contact and operational conditions differ. A proof of concept of such claim was shown in previous studies (Cabboi et al., 2016; Cabboi and Woodhouse, 2018, 2020), where experimental results obtained from a novel test setup, capable of highlighting the influence of a vibratory load on the friction force, led to the conclusion that a frequency dependent friction model is needed for specific pairs of materials in contact. Specifically, a rate-and-state model of the Dieterich–Ruina type, enhanced by means of a contact stiffness parameter, was needed to match the experimental results. However, the parameter estimation of a rate-and-state friction model is still a tedious and non-homologated process, and the need of a rate-and-state model seems currently restricted to specific operational conditions such as low velocities or perturbed states of continuous sliding, or to cases in which significant variations of the interface property may lead to alterations of the friction force during the sliding or sticking regime. It was observed that during a cyclic two-stop motion, a state variable representative of an ageing law, will cause friction variations during the sticking phase and for very short traits at the onset of sliding characterized by low velocities. This raises the question on whether or not a rate-and-state dependent friction law would be needed at all to accurately predict the cyclic stick–slip response of a forced single degree of freedom oscillator. To answer this question, first the rate-dependent law shown in Eq. (21) was assumed as the reference constitutive law for the friction force. Subsequently, predictions were carried out to obtain the cyclic response of the system shown in Fig. 1. In parallel, two further 1-DOF models were set up, in which the friction force follows the two versions of the Amontons–Coulomb model described earlier. For both models, the goal consists in finding the optimal value of the static and kinetic friction coefficient able to mimic as accurate as possible the cyclic response obtained by using a rate-dependent friction law. As mentioned earlier, only the parameter space for which $(\bar{b}-\bar{a}) \geq 0$ was explored. For the optimization concerning the rate-dependent friction force, a two-stop motion and a case of more than two stops were investigated. Subsequently, a two-stop motion was simulated again for which the rate-and-state version of the Dieterich–Ruina law was used.

To find the optimal coefficients of friction $\hat{\boldsymbol{\mu}} = [\hat{\mu}_s, \hat{\mu}_k]$ of the Amontons–Coulomb model, based on the sensitivity results obtained in the previous section, a cost function J representative of the differences between the velocities and displacements within one period of oscillation between the rate-dependent (or rate-and-state) and the Amontons–Coulomb type friction oscillator is proposed. The optimal coefficients $\hat{\boldsymbol{\mu}}$ are found as:

$$\hat{\boldsymbol{\mu}} = \arg\min_{\boldsymbol{\mu}} J \quad \text{where}$$

$$J = \sqrt{\frac{1}{2N_p}\left[\frac{\sum_{i=1}^{N_p}(\bar{x}_{r_i}-\bar{x}_{c_i})^2}{\max(\bar{x}_{r_i}^2)} + \frac{\sum_{i=1}^{N_p}(\bar{v}_{r_i}-\bar{v}_{c_i})^2}{\max(\bar{v}_{r_i}^2)}\right]} \tag{25}$$

where the subscript r refers to the dynamic response of the rate-dependent (or rate-and-state) friction oscillator, assumed as reference value, and the subscript c stands for the Amontons–Coulomb type oscillator. The parameter N_p defines the number of data points within one oscillation cycle. A constrained nonlinear optimization is carried out by introducing a physics-based constraint. Such constraint enforces the time lag between the dynamic forcing and the corresponding response obtained with the two types of oscillators to be close to zero. This constraint reads as follows

$$|\phi_r - \phi_c| = 0 \tag{26}$$

where ϕ_r and ϕ_c are the two phase angles (phase angle of the Dieterich–Ruina and Amontons–Coulomb friction oscillator, respectively). For a given friction law, Eq. (26) is computed as the difference of the phase

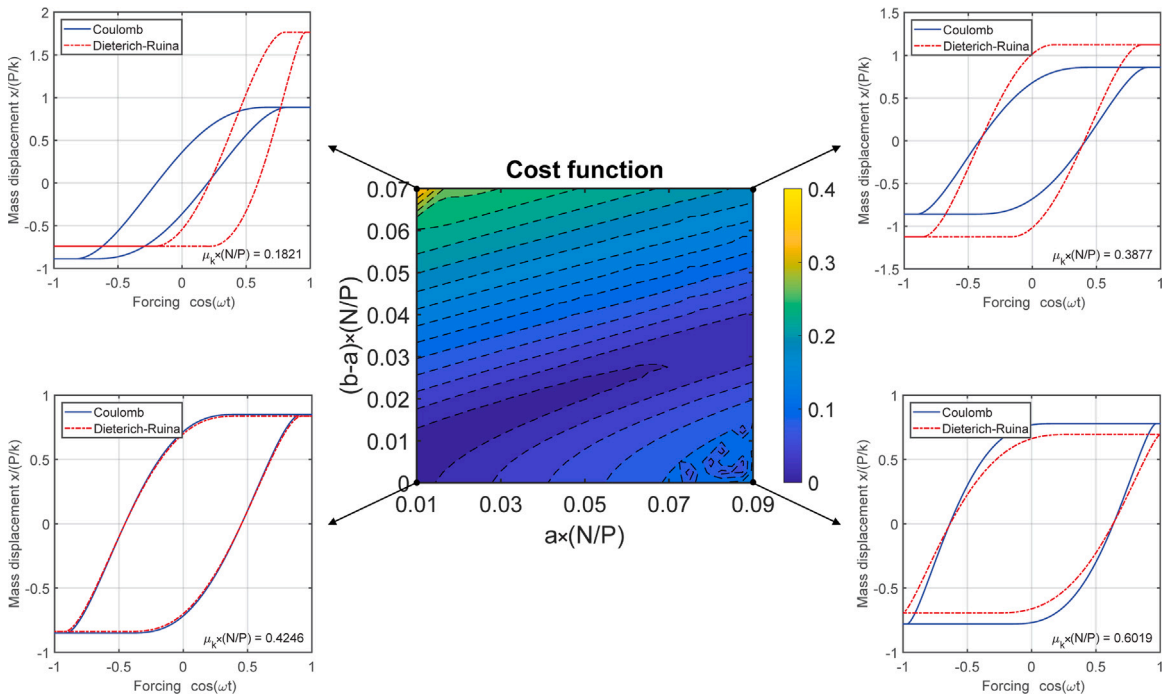

Fig. 15. Cost function obtained for optimal values of $\bar{\mu}_k$ of the Amontons–Coulomb friction ($\bar{\mu}_s = \bar{\mu}_k$) model for $r = 0.3$ and $\bar{\mu}_* = 0.4$ (two-stop stick–slip motion with Dieterich–Ruina law). Comparison of the dynamic forcing–dynamic displacement graph obtained with the Amontons–Coulomb law's ($\bar{\mu}_s = \bar{\mu}_k$) and Dieterich–Ruina law at the 4 corners of the parameter space.

angles (obtained from a Fast Frequency Transform of the time domain signal) of the excitation and of the cyclic response signals evaluated at the excitation frequency.

The constrained nonlinear optimization was carried out with the Matlab function *fmincon* and selecting the Sequential Quadratic Programming algorithm (MATLAB, 2020). N_p is set to 6283 (given a period of 2π and $d\tau = 0.001$). To avoid the identification of a local minimum of the objective function, a multi-start approach was implemented. The initial values of the nonlinear constrained optimizations were set to $\bar{\mu}_k = \bar{\mu}_*$ and with $\bar{\mu}_s$ as obtained with Eq. (19). Moreover, 5 randomly generated pairs of $\bar{\mu}_s$ and $\bar{\mu}_k$ are considered. The optimal pair of values selected is the one minimizing the objective function across the 6 initial values. For the Amontons–Coulomb type oscillator for which one single friction coefficient is considered, such as $\bar{\mu}_s = \bar{\mu}_k$, the same nonlinear constrained optimization is carried out, with the goal of identifying one single friction coefficient that best represents the reference steady-state response.

3.2. Predictive performance of the Amontons-Coulomb law

The predictive performance of the Amontons–Coulomb law is investigated for the cases of two-stop motion and more than two stops motion obtained with the steady-state version of the Dieterich–Ruina law. The parameter space explored is $0.01 \leq \bar{a} \leq 0.09$ and $0 \leq (\bar{b} - \bar{a}) \leq 0.07$, while the other parameters are kept fixed at the reference values indicated in Table 1.

3.2.1. Two-stop motion assuming the steady-state version of the Dieterich-Ruina law

The cost function obtained for the optimal values of $\bar{\mu}_k$ (when $\bar{\mu}_s = \bar{\mu}_k$) attained over the parameter space for $r = 0.3$ and $\bar{\mu}_* = 0.4$ for a two-stop stick–slip motion is shown in Fig. 15. To generate the cost function results, the parameters $\bar{a}$ and $(\bar{b} - \bar{a})$ were step-wisely incremented by a factor of 0.0025.

To facilitate the interpretation of the contour plots, for each corner of the investigated domain the corresponding dynamic hysteresis graph is shown. It is possible to observe that when the cost function is nearly zero (left-bottom corner), the optimal friction coefficient yields a very good approximation of the hysteresis graph obtained with the steady-state version of the Dieterich–Ruina law. This is an expected result, since for values of $\bar{a}$ and $(\bar{b} - \bar{a})$ tending towards zero, the dominant term in the Dieterich–Ruina law is $\bar{\mu}_*$, which resembles the Amontons–Coulomb law. On the contrary, higher values of the cost function can be observed on the top part and on the bottom right corner, which also correspond to mismatches between the dynamic hysteresis graphs. In fact, in the bottom-right corner of the parameter space, corresponding to large values of the parameter $\bar{a}$ and small values of $(\bar{b} - \bar{a})$, the optimal Amontons–Coulomb hysteresis curve exhibits an anti-clockwise rotation with respect to the Dieterich–Ruina curve, with stops occurring at a larger absolute value of the mass displacement. The opposite behaviour is instead achieved for larger values of the parameter $(\bar{b} - \bar{a})$, as shown by the top-right graph. The observed deviation is due to the difference between the optimal parameter $\hat{\mu}_k = \hat{\mu}_s$ and the value of $\bar{\mu}_s$ given by steady-state version of the Dieterich–Ruina law at $\bar{v} = 0$ (see Eq. (19), with $\hat{\mu}_s$ resulting in a higher value in the bottom-right graph and a lower value in the top-right case. It is important to note here that the bottom-right corner of the contour plot defines a parameter space for which the set of model parameters generates a friction–velocity curve predicting values of $\bar{\mu}(\bar{v})$ higher than $\bar{\mu}_s$ for most values of the velocity $\bar{v}$. This explains the higher identified value of $\hat{\mu}_k$, attempting to fit the whole branch of the friction–velocity curve. Finally, small values of $\bar{a}$, associated with large values of $(\bar{b} - \bar{a})$, can lead to asymmetric cyclic responses, which cannot be reproduced using a single Amontons–Coulomb friction coefficient, as depicted in the top-left graph. The latter parameter space implies a significant drop between the static and kinetic coefficients of friction predicted by the Dieterich–Ruina law, as illustrated previously in Fig. 9a.

To clarify the above points, the variation of $\bar{\mu}(\bar{v})$ (as defined in Eq. (21)), is shown with reference to two arbitrary directions within the explored parameter space. In Fig. 16, the horizontal and the vertical line overlaying the contour plot define a set of parameters where either $(\bar{b} - \bar{a})$ or $\bar{a}$ are kept constant while varying the other one. Following

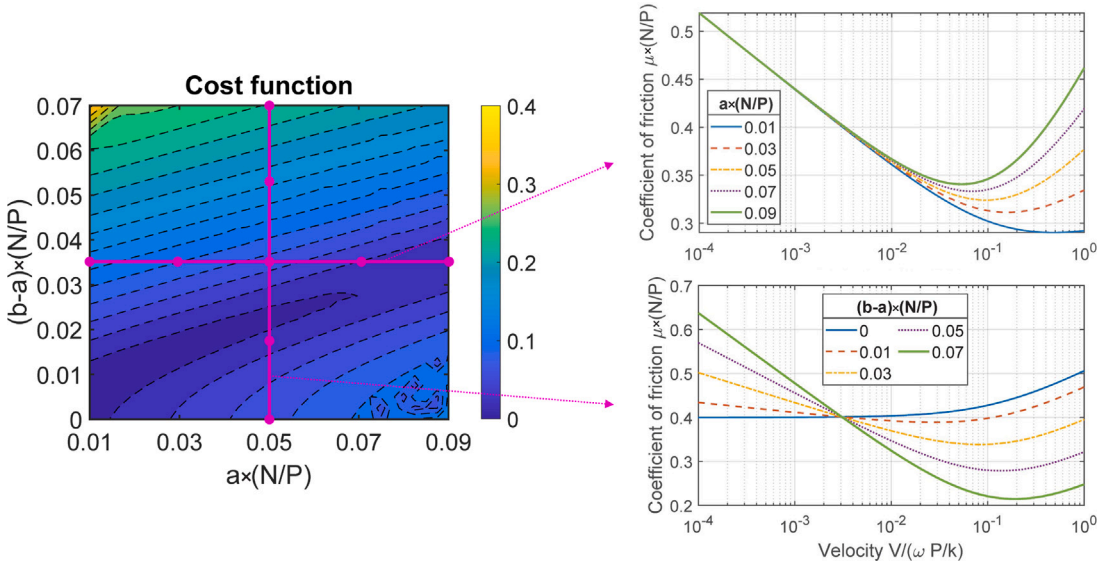

Fig. 16. Cost function obtained for optimal values of $\bar{\mu}_k$ of the Amontons–Coulomb friction ($\bar{\mu}_s = \bar{\mu}_k$) model for $r = 0.3$ and $\bar{\mu}_* = 0.4$ (two-stop stick–slip motion with steady-state version of the Dieterich–Ruina law) and corresponding $\bar{\mu}(\bar{v})$ curves obtained by either fixing $\bar{a}$ (vertical pink line) or $(\bar{b} - \bar{a})$ (horizontal pink line). (For interpretation of the references to colour in this figure legend, the reader is referred to the web version of this article.)

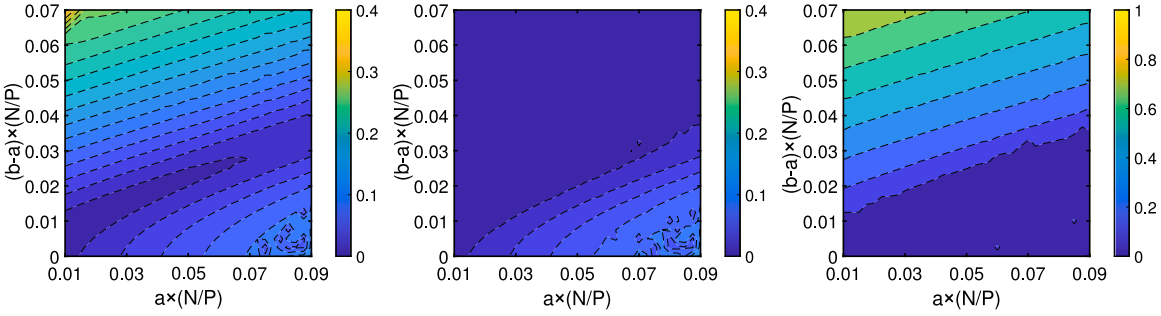

(a) Cost function for $\bar{\mu}_s = \bar{\mu}_k$ (b) Cost function for $\bar{\mu}_s \geq \bar{\mu}_k$ (c) Difference $\bar{\mu}_s - \bar{\mu}_k$

Fig. 17. Cost function obtained for optimal values of $\bar{\mu}_k$ and $\bar{\mu}_s$ of the Amontons–Coulomb friction model for $r = 0.3$ and $\bar{\mu}_* = 0.4$ (two-stop motion with steady-state version of the Dieterich–Ruina law), considering $\bar{\mu}_s = \bar{\mu}_k$ (subfigure (a)) or $\bar{\mu}_s \geq \bar{\mu}_k$ (subfigure (b)). The difference between the optimal values of $\bar{\mu}_k$ and $\bar{\mu}_s$ is shown in (subfigure (c)). (For interpretation of the references to colour in this figure legend, the reader is referred to the web version of this article.)

the vertical line, it is possible to observe that for decreasing values of $(\bar{b} - \bar{a})$, the slope of the friction–velocity curves tends to decrease, gradually flattening the curve. As mentioned earlier, for low $(\bar{b} - \bar{a})$ and for specific values of $\bar{a}$, Eq. (21) reproduces cases in which $\bar{\mu}(\bar{v})$ tends to be higher than $\bar{\mu}_s$. With reference to the horizontal line, it is possible to appreciate that the non-monotonicity of the friction curve is emphasized for increasing values of $\bar{a}$.

It can be concluded that the Amontons–Coulomb model with $\bar{\mu}_s = \bar{\mu}_k$ is capable of reproducing the steady-state version of the Dieterich–Ruina results for the cyclic response of 1-DOF oscillator only in a very limited region of the parameter space, corresponding to low values of both $\bar{a}$ and $(\bar{b} - \bar{a})$. The latter set of model parameters define friction–velocity curves that tend to be flat and scarcely velocity dependent, characterized by a small drop between the static and kinetic friction coefficients.

The cost function obtained for the optimal values of $\bar{\mu}_k$ and $\bar{\mu}_s$ (when $\bar{\mu}_s \geq \bar{\mu}_k$) attained over the parameter space for $r = 0.3$ and $\bar{\mu}_* = 0.4$ for the same two-stop motion is shown in Fig. 17b. By direct comparison with Fig. 17a (obtained for $\bar{\mu}_s = \bar{\mu}_k$), it is possible to observe that this type of Amontons–Coulomb friction model extends by far the region of the cost function showing errors close to zero. Therefore, this model would yield a much better approximation of the dynamic forcing–displacement graph obtained with the steady-state version of the Dieterich–Ruina law. In Fig. 17c, where the difference between the optimal values of $\bar{\mu}_k$ and $\bar{\mu}_s$ is reported, it is confirmed that this better approximation is indeed achieved in the region where the difference between $\hat{\mu}_k$ and $\hat{\mu}_s$ is more pronounced and, in particular, this difference gradually increases moving towards the top-left corner of the parameter space. Recalling the effect of the static friction coefficient on the dynamic forcing–displacement curves (see anticlockwise rotations in Fig. 4), it can be deduced that larger values of $\bar{\mu}_s$ allow to improve the mismatch between curves observed in the top-right corner of Fig. 15. Even asymmetric behaviours as those shown in the top-left corner of the same figure can be obtained using very different values of $\bar{\mu}_k$ and $\bar{\mu}_s$, as also discussed in Csernak and Licsko (2021). Nonetheless, even different values of the kinetic and static friction coefficients cannot yield a good approximation of the Dieterich–Ruina results for large values of $\bar{a}$ and small $(\bar{b} - \bar{a})$. The reason of being that was already explained with the reference to Fig. 16.

3.2.2. *Two-stop motion assuming the rate-and-state version of the Dieterich-Ruina law*

To complete the comparative analysis for the two-stop motion, the complete rate-and-state friction law was used, for which the predictive performance of the Amontons–Coulomb is assessed. The corresponding cost function is illustrated in Fig. 18, and was obtained for assuming $r = 0.3$ and $\bar{\mu}_* = 0.4$. The pattern displayed by the resulting cost functions are clearly more complicated than those obtained for the

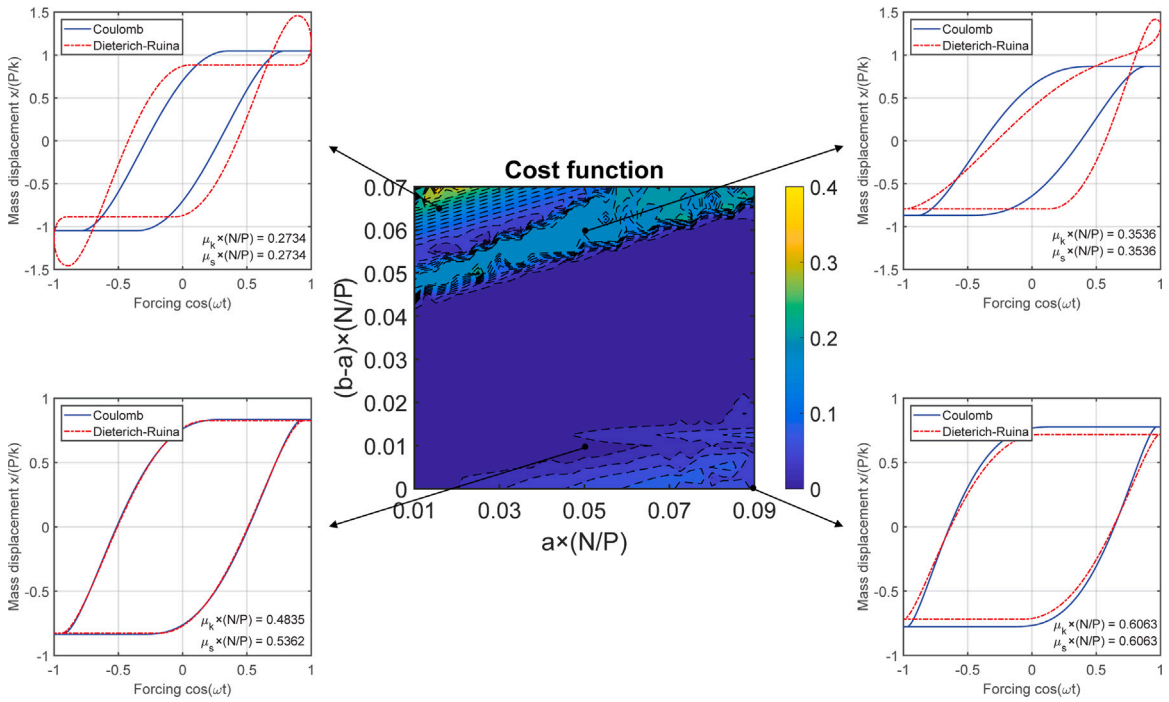

Fig. 18. Cost function obtained for optimal values of $\bar{\mu}_k$ and $\bar{\mu}_s$ of the Amontons–Coulomb friction model for $r = 0.3$ and $\bar{\mu}_* = 0.4$ (two-stop motion with rate-and-state Dieterich–Ruina law), considering $\mu_s \geq \mu_k$. Comparison of the dynamic forcing–dynamic displacement graph obtained with the Amontons–Coulomb law ($\bar{\mu}_s \geq \bar{\mu}_k$) and rate-and-state Dieterich–Ruina law at 4 points of the parameter space.

same values of r and $\bar{\mu}_*$ disregarding the effect of the state variable θ, and shown in Fig. 17b. Nonetheless, the Amontons–Coulomb law is still able to reproduce the cyclic two-stop motion obtained using the Dieterich–Ruina law in a wide region of the parameter space. Moreover, the presence of the state variable leads to a slightly better agreement between the responses in the bottom-right region of the parameter space, for which the Amontons–Coulomb law failed to reproduce the responses obtained by means of the steady-state version of the Dieterich–Ruina law. In fact, as discussed in Section 3.2.1, in this region the steady-state version of the Dieterich–Ruina law produces values of $\bar{\mu}(\bar{v})$ larger than $\bar{\mu}_s$ for higher sliding velocities. While the Amontons–Coulomb law cannot reproduce such a behaviour, in the presence of the state variable θ this effect is attenuated by the gradual increase of the static friction coefficient during the sticking phases. This explains the improved match between the two hysteresis graphs, highlighted in the bottom-left and in the bottom-right of Fig. 18. Note that the optimal values of $\bar{\mu}_k$ and $\bar{\mu}_s$ (with $\bar{\mu}_s \geq \bar{\mu}_s$) are represented as well within each hysteresis graph. With reference to the hysteresis plot displayed at the bottom right, $\bar{\mu}_k$ and $\bar{\mu}_s$ tend to be equal, highlighting the profound effect of θ in increasing the value of the static friction during the sticking phases.

Differently from what observed in Fig. 17b, the top-left region of the parameter space presents a significant mismatch between the two force–displacements graphs. As shown in the top-right hysteresis plot, corresponding to the light blue region, the rate-and-state responses become strongly asymmetric, exhibiting only one stop per cycle. Such type of response cannot be reproduced by the Amontons–Coulomb law. Slightly better agreements are obtained moving towards the top-left corner, where the symmetry of the rate-and-state response is recovered. However, these responses are still characterized by complicated patterns which cannot be fully reproduced by the Amontons–Coulomb law. In conclusion, the Amontons–Coulomb law can be used to reproduce the two-stop motion results obtained by the Dieterich–Ruina law in a wide region of the parameter space also when the state variable θ is taken into account. However, the mismatch between the responses obtained using these two laws rapidly increases moving towards higher values of $(\bar{b} - \bar{a})$, particularly for small values of $\bar{a}$. In fact, the effect of the state variable becomes more and more significant as $\bar{b}$ is increased, leading to more complicated patterns in the cyclic responses.

3.2.3. More than two stops for the steady-state version of the Dieterich-Ruina law

The performance of the Amontons–Coulomb law for describing a stick–slip motion covering more than two stops within one cycle obtained with the steady-state version of the Dieterich–Ruina law is investigated in Fig. 19. The cost functions obtained for the optimal values of $\bar{\mu}_k$ and $\bar{\mu}_s$ (when $\bar{\mu}_s = \bar{\mu}_k$ (a) and when $\bar{\mu}_s \geq \bar{\mu}_k$ (b)) attained over the parameter space for $r = 0.1$ and $\bar{\mu}_* = 0.2$, together with the difference between the optimal values of $\bar{\mu}_k$ and $\bar{\mu}_s$ (Fig. 19c) are investigated. Despite the larger complexity of the patterns displayed by the values of the cost function, it is still possible to observe that, while the Amontons–Coulomb friction model with $\bar{\mu}_s = \bar{\mu}_k$ is mostly unable to reproduce results obtained for a rate-dependent friction law, an improved match is still achieved by different $\bar{\mu}_k$ and $\bar{\mu}_s$ in a confined region located on the centre-left and top-right side of the parameter space. It is worth mentioning that the top-left corner of the parameter space investigated in Figs. 19 and 20 is not reported here since negative values $\bar{\mu}$ from the rate-dependent friction law were obtained, in accordance with the condition expressed in Eq. (20).

The comparison of the dynamic forcing–displacement graph obtained with the Amontons–Coulomb law ($\bar{\mu}_s \geq \bar{\mu}_k$) and with the steady-state version of the Dieterich–Ruina law is shown in Fig. 20 for four different pairs of $(\bar{b} - \bar{a})$ and $\bar{a}$ selected from the parameter space. Note that depending on $\bar{a}$ and $(\bar{b} - \bar{a})$, different number of stops will be observed with the Dieterich–Ruina law; this indeed explains the more complicated patterns shown by the values of the cost function with respect to the previously investigated two-stop case. Moreover, an explanation is provided for the presence of two main regions of the parameter space where it is possible or not possible, respectively, to approximate the rate-dependent behaviour using the Amontons–Coulomb model. It is shown that, below the boundary separating these two regions, intermediate stops are no longer achieved by the

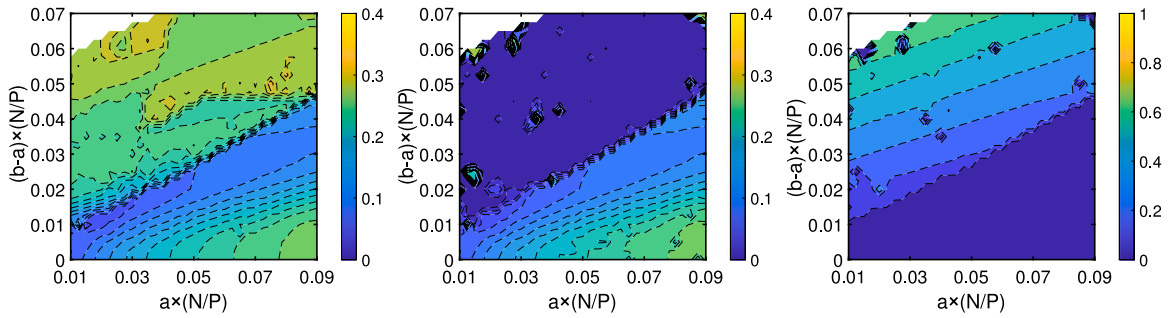

(a) Cost function for $\bar{\mu}_s = \bar{\mu}_k$ (b) Cost function for $\bar{\mu}_s \geq \bar{\mu}_k$ (c) Difference $\bar{\mu}_s - \bar{\mu}_k$

Fig. 19. Cost function obtained for optimal values of $\bar{\mu}_k$ and $\bar{\mu}_s$ of the Amontons–Coulomb friction model for $r = 0.1$ and $\bar{\mu}_* = 0.2$ (more than two stops stick–slip motion with the Dieterich–Ruina law), considering $\bar{\mu}_s = \bar{\mu}_k$ (subfigure (a)) or $\bar{\mu}_s \geq \bar{\mu}_k$ (subfigure (b)). The difference between the optimal values of $\bar{\mu}_k$ and $\bar{\mu}_s$ is shown in (subfigure (c)).

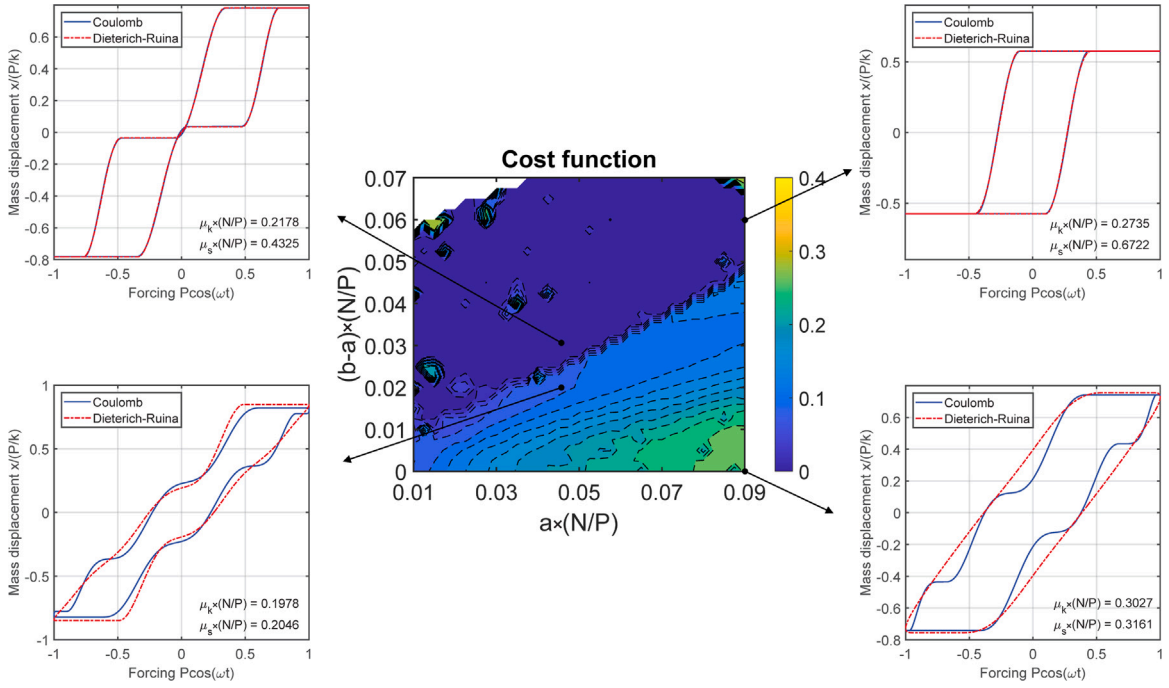

Fig. 20. Cost function obtained for optimal values of $\bar{\mu}_k$ and $\bar{\mu}_s$ of the Amontons–Coulomb friction model for $r = 0.1$ and $\bar{\mu}_* = 0.2$ (more than two stops stick–slip motion with Dieterich–Ruina law), considering $\mu_s \geq \mu_k$. Comparison of the dynamic forcing–dynamic displacement graph obtained with the Amontons–Coulomb law ($\bar{\mu}_s \geq \bar{\mu}_k$) and Dieterich–Ruina law at 4 points of the parameter space.

Dieterich–Ruina law, leading to a smoothening effect which cannot be reproduced by Amontons–Coulomb model. This effect becomes stronger and stronger moving towards the bottom-right corner of the parameter space. This behaviour is due to the trend observed in Fig. 16, showing that for a set of model parameters it is possible to reproduce friction curves for which $\bar{\mu}(\bar{v})$ tends to be higher than $\bar{\mu}_s$. As noted before, it can be concluded that, also when more than two stops are present within a response cycle, the Amontons–Coulomb law cannot be used to approximate the Dieterich–Ruina results when $\bar{a}$ is large and $(\bar{b} - \bar{a})$ is small.

4. Discussion and conclusions

4.1. Significance of the results

The relevance of the obtained results needs to be assessed with reference to both the "forward" and "inverse" problem concerning friction modelling and identification. As far as the forward problem concerns, and in case the underlining friction law is constituted by a rate-dependent friction law, the output of this study clearly shows that to reliably predict the cyclic response of a two-stop motion of a 1-DOF system, a set of Amontons–Coulomb coefficients representing the static and kinetic friction can be enough. The only region of the explored parameter space for which the Amontons–Coulomb coefficients fail to reliably predict the cyclic response refers to cases for which the steady-state version of the Dieterich–Ruina law reproduces values of $\mu(v)$ higher than the static coefficient. Note that, even if counter-intuitive, increasing trends of such kind were experimentally identified (Wiercigroch et al., 1999; Wojewoda et al., 2008) and linked to the non-reversibility of the friction–velocity curves. On top of that, a recent study (Cabboi and Woodhouse, 2018) also reported significant increases of the kinetic friction coefficients (from 0.4 to 0.7 for polycarbonate pins on steel disc) for increasing values of sliding velocities. The true physical mechanisms behind such counter-intuitive trends are still unclear, and any discussion on such matter falls outside the scope of this study. When the underling friction law is constituted by the described rate-and-state friction law, the use of a pair of Amontons–Coulomb coefficients may only be justified for a confined region of the parameter space formed by limited combinations of $(\bar{b} - \bar{a})$ and $\bar{a}$. If more than two stops within a cyclic response are simulated by

means of a rate-dependent friction law, the quality of the fit with a pair of Amontons–Coulomb coefficients decreases. It is worth highlighting here that the prediction performance of the Amontons–Coulomb coefficients would decrease even more if the reference response would be simulated by assuming a rate-and-state friction law. Note that to increase the number of stops within one cycle, the parameters r and $\bar{\mu}_*$ were decreased. However, more than two stops could also be obtained by assuming a dynamic variation of the normal force during the cyclic response. Under such operational conditions, a rate-and-state model including an additional state variable that accounts for a non-trivial dependence between the normal force and the friction force should be used (see Linker and Dieterich, 1992; Prakash, 1998; Tal et al., 2020). For the latter case, in the authors' opinion, a pair of Amontons–Coulomb coefficients would not be enough to capture the cyclic response in a reliable way.

It is also worth mentioning that in the presented study, no tangential contact stiffness was included, accounting for eventual micro-slip (pre-sliding) phenomenon occurring during the transition from stick to slip. In principle, the presence or not of the contact stiffness should not alter the presented conclusions, since for both friction laws (Amontons–Coulomb and Dieterich–Ruina), an equivalent formulation representative of the contact stiffness can simply be added to mimic the partial-slip cases.

Concerning the inverse problem, the obtained results have a profound implication for the correct identification of friction laws. Since the explored parameter space shows regions for which the friction laws are almost indistinguishable, it is counter-advised to use the cyclic response to identify the underlining friction law of a sliding system. Attempts of identifying friction laws, based only on the cyclic response, could lead to misleading conclusions concerning the characterization of the inherent constitutive friction law. Note though that Figs. 3c, 4c, 13c and 14c show a clear feature, with reference to the rotation of the dynamic forcing vs displacement curves, that seems unique to the chosen friction law. The rotations observed in Figs. 13c and 14c seem to be ascribable to a velocity dependence of the friction law. Nonetheless, it is still unclear on how robust such a feature may be during actual experiment runs. In a similar fashion, a further discriminating feature may be given by the friction-force vs velocity graphs (see Fig. 11a), if measurable during an experiment in which stick–slip is present. Any discrepancy between the acceleration and deceleration traits calls for an additional state variable within the friction law.

A final note is devoted to the regularization of the Dieterich–Ruina law for velocity reversals. The modified version enables its use for simulations and optimization runs in which velocity reversals and stick events are present. However, its capability of predicting the static friction coefficient is undoubtedly questionable and no comparison was performed with experimental data.

4.2. Conclusions

The comparative study started with a sensitivity analysis on the stick–slip cyclic responses of a single degree of freedom system in frictional contact to the ground. Three friction laws were compared, the Amontons–Coulomb law and two versions of a regularized Dieterich–Ruina friction law: the steady-state and rate-and-state version. Once the most meaningful model parameters were identified, the results of the sensitivity study highlighted three distinguished features occurring during one cycle for a two-stop motion: (a) variations of the maximum amplitude of displacement and velocity; (b) an enlargement (or shrinkage) of the area defined by the dynamic forcing vs displacement curve; (c) a rotation of the dynamic forcing vs displacement curve. Feature (a) was observed for all investigated cases, while feature (b) and (c) were separately observed for the case of using a single coefficient of friction and for the case characterized by a distinct pair of Amontons–Coulomb coefficients, μ_s and μ_k, respectively. Concerning the Dieterich–Ruina law, features (b) and (c) merged into a combined effect on the cyclic response if a steady-state version of the Dieterich–Ruina law was used, while case (c) was still observable if the rate-and-state friction law was assumed.

The comparative analysis was finalized through an optimization study, with the aim of identifying the parameter space for which the Amontons–Coulomb law can reliably be used to predict a stick–slip cyclic response. For this study, a cost function expressed in terms of the displacement and velocity response differences and a constraint based on the phase difference were introduced, and the Dieterich–Ruina laws were assumed as the underlining constitutive laws of friction. When a steady-state version of the Dieterich–Ruina law was used, the optimization results showed that for a large region of the investigated parameter space, the predictive performance for stick–slip response of the Amontons–Coulomb law (in case of two stops), is fairly similar to the one obtained by using the Dieterich–Ruina law. Significant mismatches between the two laws were observed for a region in the Dieterich–Ruina parameter space that tends to generate friction–velocity curves with a pronounced velocity-strengthening trend, leading to coefficients of kinetic friction higher than the static one. When a rate-and-state version is used, the mismatch with the responses generated by assuming a pair of Amontons–Coulomb coefficients increases. Such mismatch increases even more, in case of more than two stops during one stick–slip cycle.

CRediT authorship contribution statement

Alessandro Cabboi: Conceptualization, Methodology, Investigation, Formal analysis, Writing – original draft, Writing – review & editing, Visualization. **Luca Marino:** Investigation, Software, Data curation, Formal analysis, Visualization, Writing – review & editing. **Alice Cicirello:** Conceptualization, Methodology, Writing – review & editing.

Declaration of competing interest

The authors declare that they have no known competing financial interests or personal relationships that could have appeared to influence the work reported in this paper.

Data availability

Data will be made available on request.

Appendix

Algorithm 1 Numerical integration approach for 1-DOF systems with Coulomb/rate-dependent friction

1: $\bar{x}_0$, $\bar{x}'_0$, N_{cyc} ← Initial position and velocity, number of excitation periods
2: $\tau_0 \leftarrow 0$, $\tau_f \leftarrow 2\pi N_{cyc}$ ▷ Set initial and final simulation time
3: $\tau \leftarrow \tau_0$, $\bar{x} \leftarrow \bar{x}_0$, $\bar{x}' \leftarrow \bar{x}'_0$ ▷ Initialize time, position and velocity vectors
4: **while** $\tau_0 \leq \tau_f$ **do**
5: **if** $|\cos(\tau_0) - \bar{x}_0| \geq \bar{\mu}_s$ **then** ▷ Sliding phase
6: Integrate Eq.(3) with ode45 ▷ $\bar{\mu}(\bar{x}')$ from Eq.(6)(a) [Coulomb] or Eq.(21)(a) [rate-dependent]
7: Terminate integration when $\bar{x}' = 0$ ▷ Event condition
8: Update vectors τ, $\bar{x}$, $\bar{x}'$ with integration results
9: **else** ▷ Sticking phase
10: Find $\tau_1 : |\cos(\tau_1) - \bar{x}_0| - \bar{\mu}_s = 0$ ▷ Determine when the stop terminates
11: Set $\bar{x}_1 = \bar{x}_0$, $\bar{x}'_1 = 0$ ▷ Position and velocity remain constant during the stop
12: **end if**
13: Set τ_0, $\bar{x}_0$, $\bar{x}'_0$ to final time, position and velocity of the current phase
14: **end while**

Algorithm 2 Numerical integration approach for 1-DOF systems with rate-and-state friction

1: $\bar{x}_0$, $\bar{x}'_0$, $\bar{\theta}_0$, N_{cyc} ← Initial position, velocity and state, number of excitation periods
2: $\tau_0 \leftarrow 0$, $\tau_f \leftarrow 2\pi N_{cyc}$ ▷ Set initial and final simulation time
3: $\tau \leftarrow \tau_0$, $\bar{x} \leftarrow \bar{x}_0$, $\bar{x}' \leftarrow \bar{x}'_0$, $\bar{\theta} \leftarrow \bar{\theta}_0$ ▷ Initialize time, position, velocity and state vectors
4: **while** $\tau_0 \leq \tau_f$ **do**
5: **if** $|\cos(\tau_0) - \bar{x}_0| \geq \bar{\mu}_s(\bar{\theta}_0, 0)$ **then** ▷ Sliding phase, $\bar{\mu}_s(\bar{\theta}_0, \Delta\tau)$ from Eq.(14)
6: Integrate Eqs.(3) and (9) with ode23s ▷ $\bar{\mu}(\bar{x}', \bar{\theta})$ from Eq.(22)(a)
7: Terminate integration when $\bar{x}' = 0$ ▷ Event condition
8: Update vectors τ, $\bar{x}$, $\bar{x}'$, $\bar{\theta}$ with integration results
9: **else** ▷ Sticking phase
10: Find $\tau_1 : |\cos(\tau_1) - \bar{x}_0| - \bar{\mu}_s(\bar{\theta}_0, \tau_1 - \tau_0) = 0$ ▷ Determine when the stop terminates
11: Set $\bar{x}_1 = \bar{x}_0$, $\bar{x}'_1 = 0$, $\bar{\theta}_1 = \bar{\theta}_0 + \tau_1 - \tau_0$ ▷ State increases linearly during the stop
12: **end if**
13: Set τ_0, $\bar{x}_0$, $\bar{x}'_0$, $\bar{\theta}_0$ to final time, position, velocity and state of the current phase
14: **end while**

References

Al-Bender, F., Lampaert, V., Swevers, J., 2005. The generalized Maxwell-slip model: a novel model for friction Simulation and compensation. IEEE Trans. Automat. Control 50 (11), 1883–1887.

Bar-Sinai, Y., Spatschek, R., Brener, E.A., Bouchbinder, E., 2015. Velocity-strengthening friction significantly affects interfacial dynamics, strength and dissipation. Sci. Rep. 5, 7841.

Berger, E.J., 2002. Friction modeling for dynamic system simulation. Appl. Mech. Rev. 55 (6), 535–577.

Blau, P.J., 2009. Friction Science and Tecnology: From Concepts to Applications. CRC Press, Taylor and Francis, Boca Raton, USA.

Bureau, L., Baumberger, T., Caroli, C., 2002. Rheological aging and rejuvenation in solid friction contacts. Eur. Phys. J. E 8 (3), 331–337.

Cabboi, A., Putelat, T., Woodhouse, J., 2016. The frequency response of dynamic friction: Enhanced rate-and-state models. J. Mech. Phys. Solids 92, 210–236.

Cabboi, A., Woodhouse, J., 2018. Validation of a constitutive law for friction-induced vibration under different wear conditions. Wear 396–397, 107–125.

Cabboi, A., Woodhouse, J., 2020. Identifying short-term variation of dynamic friction by means of its frequency response function. J. Sound Vib. 472 (115212).

Csernak, G., Licsko, G., 2021. Asymmetric and chaotic responses of dry friction oscillators with different static and kinetic coefficients of friction. Meccanica 56, 2401–2414.

Den Hartog, J.P., 1931. Forced vibrations with combined viscous and Coulomb damping. Trans. Am. Soc. Mech. Eng. 53, 107–115.

Dieterich, J.H., 1979. Modeling rock friction: 1. Experimental results and constitutive equations. J. Geophys. Res.: Solid Earth 84 (B5), 2161–2168.

Dupont, P., Hayward, V., Armstrong, B., Altpeter, F., 2002. Single state elastoplastic friction models. IEEE Trans. Automat. Control 47 (5), 787–792.

Elmer, F.-J., 1997. Nonlinear dynamics of dry friction. J. Phys. A: Math. Gen. 30 (17), 6057–6063.

Gagnon, L., Morandini, M., Ghiringhelli, G.L., 2020. A review of friction damping modeling and testing. Arch. Appl. Mech. 90, 107–126.

Gastaldi, C., Gola, M.M., 2016. On the relevance of a microslip contact model for under-platform dampers. Int. J. Mech. Sci. 115–116, 145–156.

Gonthier, Y., Lange, C., Piedboeuf, J.-C., McPhee, J., Lange, C., 2004. A regularized contact model with asymmetric damping and dwell-time dependent friction. Multibody Syst. Dyn. 11 (3), 209–233.

Heslot, F., Baumberger, T., Perrin, B., Caroli, B., Caroli, C., 1994. Creep, stick-slip, and dry-friction dynamics: experiments and a heuristic model. Phys. Rev. E 49, 4973–4988.

Hess, D.P., Soom, H., 1990. Friction at a lubricated line contact operating at oscillating sliding velocities. J. Tribol. 112 (1), 147–152.

Hong, H.K., Liu, C.S., 2000. Coulomb friction oscillator: modelling and responses to harmonic loads and base excitations. J. Sound Vib. 229 (5), 1171–1192.

Hong, H.K., Liu, C.S., 2001. Non-sticking oscillation formulae for Coulomb friction under harmonic loading. J. Sound Vib. 244 (5), 883–898.

Jankowski, K., Saha, A., Stefański, A., 2016. Introduction of novel model of friction and analysis of presliding domain of friction with non-local memory effect based upon Maxwell slip model structures. Tribol. Int. 102, 378–391.

Lacerra, G., Di Bartolomeo, M., Milana, S., Baillet, L., Chatelet, E., Massi, F., 2018. Validation of a new frictional law for simulating friction-induced vibrations of rough surfaces. Tribol. Int. 121, 468–480.

Lampaert, V., Al-Bender, F., Swevers, J., 2004. Experimental characterization of dry friction at low velocities on a developed tribometer setup for macroscopic measurements. Tribol. Lett. 16, 95–105.

Laursen, T.A., 1998. Computational Contact and Impact Mechanics: Fundamentals of Modeling Interfacial Phenomena in Nonlinear Finite Element Analysis. Springer Berlin Heidelberg, Berlin, Heidelberg.

Le Bot, A., Scheibert, J., Vasko, A.A., Braun, O.M., 2019. Relaxation tribometry: A generic method to identify the nature of contact forces. Tribol. Lett. 67.

Linker, M.F., Dieterich, J.H., 1992. Effects of variable normal stress on rock friction: Observations and constitutive equations. J. Geophys. Res.: Solid Earth 97 (B4), 4923–4940.

Liu, L.L., Wu, Z.Y., 2014. A new identification method of the Stribeck friction model based on limit cycles. Proc. Inst. Mech. Eng. C 228 (15), 2678–2683.

Lopez, I., Nijmeijer, H., 2009. Prediction and validation of the energy dissipation of a friction damper. J. Sound Vib. 328 (4), 396–410.

Marino, L., Cicirello, A., 2020. Experimental investigation of a single-degree-of-freedom with Coulomb friction. Nonlinear Dynam. 99, 1781–1799.

Marino, L., Cicirello, A., 2021. Multi-degree-of-freedom systems with a Coulomb friction contact: analytical boundaries of motion regimes. Nonlinear Dynam. 104 (1), 35–63.

Marone, C., 1998. Laboratory-derived friction laws and their application to seismic faulting. Annu. Rev. Earth Planet. Sci. 26 (1), 643–696.

Marques, F., Flores, P., Pimenta Claro, J.C., Lankarani, H.M., 2016. A survey and comparison of several friction force models for dynamic analysis of multibody mechanical systems. Nonlinear Dynam. 86.

Marques, F., Wolinski, L., Wojtyra, M., Flores, P., Lankarani, H.M., 2021. An investigation of a novel LuGre-based friction force model. Mech. Mach. Theory 166, 104493.

MATLAB, 2020. Version 9.9.0.123456 (R2020b). The MathWorks Inc., Natick, Massachusetts.

Meng, Y., Xu, J., Jin, Z., Prakash, B., Hu, Y., 2020. A review of recent advances in tribology. Friction 8, 221–300.

Pennestrì, E., Rossi, V., Salvini, P., Valentini, P.P., 2016. Review and comparison of dry friction force models. Nonlinear Dynam. 83, 1785–1801.

Pitenis, A.A., Dowson, D., Gregory Sawyer, W., 2014. Leonardo da Vinci's friction experiments: An old story acknowledged and repeated. Tribol. Lett. 56 (3), 509–515.

Prakash, V., 1998. Frictional response of sliding interfaces subjected to time varying normal pressures. J. Tribol. 120 (1), 97–102.

Putelat, T., Dawes, J.H.P., 2015. Steady and transient sliding under rate-and-state friction. J. Mech. Phys. Solids 78, 70–93.

Putelat, T., Dawes, J.H.P., Willis, J.R., 2007. Sliding modes of two interacting frictional interfaces. J. Mech. Phys. Solids 55 (10), 2073–2105.

Rice, J.R., Ben-Zion, Y., 1996. Slip complexity in earthquake fault models. Proc. Natl. Acad. Sci. 93 (9), 3811–3818.

Rigaud, E., Perret-Liaudet, J., Belin, M., Joly-Pottuz, L., Martin, J.-M., 2010. An original dynamic tribotest to discriminate friction and viscous damping. Tribol. Int. 43 (1), 320–329.

Ruina, A.L., 1983. Slip instability and state variable friction laws. J. Geophys. Res. 88, 10359–10370.

Saha, A., Wahi, P., Wiercigroch, M., Stefański, A., 2016. A modified LuGre friction model for an accurate prediction of friction force in the pure sliding regime. Int. J. Non-Linear Mech. 80, 122–131.

Shaw, S.W., 1986. On the dynamic response of a system with dry friction. J. Sound Vib. 108 (2), 305–325.

Shroff, S.S., de Boer, M.P., 2016. Full assessment of micromachine friction within the rate–state framework: Experiments. Tribol. Lett. 63 (3).

Sorge, F., 2007. On the frequency behaviour, stability and isolation properties of dry friction oscillators. Meccanica 42 (1), 61–75.

Sun, Y.-H., Chen, T., Qiong Wu, C., Shafai, C., 2015. Comparison of four friction models: feature prediction. J. Comput. Nonlinear Dyn. 11 (3).

Tal, Y., Rubino, V., Rosakis, A.J., Lapusta, N., 2020. Illuminating the physics of dynamic friction through laboratory earthquakes on thrust faults. Proc. Natl. Acad. Sci. 117 (35), 21095–21100.

Vakis, A.I., Yastrebov, V.A., Scheibert, J., Nicola, L., Dini, D., Minfray, C., Almqvist, A., Paggi, M., Lee, S., Limbert, G., Molinari, J., Anciaux, G., Aghababaei, R., Echeverri Restrepo, S., Papangelo, A., Cammarata, A., Nicolini, P., Putignano, C., Carbone, G., Stupkiewicz, S., Lengiewicz, J., Costagliola, G., Bosia, F., Guarino, R., Pugno, N., Müser, M., Ciavarella, M., 2018. Modeling and simulation in tribology across scales: an overview. Tribol. Int. 125, 169–199.

Van De Velde, F., De Baets, P., 1998. The relation between friction force and relative speed during the slip-phase of a stick-slip cycle. Wear 219 (2), 220–226.

Vanossi, A., Manini, N., Urbakh, M., Zapperi, S., Tosatti, E., 2013. Modeling friction: From nanoscale to mesoscale. Rev. Modern Phys. 85, 529–552.

Weeks, J.D., 1993. Constitutive laws for high-velocity frictional sliding and their influence on stress drop during unstable slip. J. Geophys. Res.: Solid Earth 98 (B10), 17637–17648.
Wiercigroch, W., Sin, V.W.T., Liew, Z.F.K., 1999. Non-reversible dry friction oscillator: design and measurements. Proc. Inst. Mech. Eng. C 213 (5), 527–534.
Canudas de Wit, C., Olsson, H., Astrom, K.J., Lischinsky, P., 1995. A new model for control of systems with friction. IEEE Trans. Automat. Control 40 (3), 419–425.
Wojewoda, J., Stefański, A., Wiercigroch, M., Kapitaniak, T., 2008. Hysteretic effects of dry friction: modelling and experimental studies. Phil. Trans. R. Soc. A 366 (1866), 747–765.
Woodhouse, J., Putelat, T., McKay, A., 2015. Are there reliable models of friction? Phil. Trans. R. Soc. A 373 (2051).
Wriggers, P., 1998. Computational Contact Mechanics. Springer Berlin Heidelberg, Berlin, Heidelberg.